Title
The neural basis of heat seeking in a human-infective parasitic worm

Journal
Current Biology, 32(10)

ISSN
0960-9822

Authors
Bryant, Astra S
Ruiz, Felicitas
Lee, Joon Ha
et al.

Publication Date
2022-05-01

DOI
10.1016/j.cub.2022.04.010

Peer reviewed

HHS Public Access

Author manuscript

Curr Biol. Author manuscript; available in PMC 2023 May 23.

Published in final edited form as:

Curr Biol. 2022 May 23; 32(10): 2206–2221.e6. doi:10.1016/j.cub.2022.04.010.

The neural basis of heat seeking in a human-infective parasitic worm

Astra S. Bryant[1], **Felicitas Ruiz**[1,†], **Joon Ha Lee**[1,‡], **Elissa A. Hallem**[1,2,3,*]

[1]Department of Microbiology, Immunology, and Molecular Genetics, University of California, Los Angeles, Los Angeles, CA 90095

[2]Molecular Biology Institute, University of California, Los Angeles, Los Angeles, CA 90095

[3]Lead contact

Summary

Soil-transmitted parasitic nematodes infect over one billion people and cause devastating morbidity worldwide. Many of these parasites have infective larvae that locate hosts using thermal cues. Here, we identify the thermosensory neurons of the human threadworm *Strongyloides stercoralis* and show that they display unique functional adaptations that enable the precise encoding of temperatures up to human body temperature. We demonstrate that experience-dependent thermal plasticity regulates the dynamic range of these neurons while preserving their ability to encode host-relevant temperatures. We describe a novel behavior in which infective larvae spontaneously reverse attraction to heat sources at sub-body temperatures and show that this behavior is mediated by rapid adaptation of the thermosensory neurons. Finally, we identify thermoreceptors that confer parasite-specific sensitivity to body heat. Our results pinpoint the parasite-specific neural adaptations that enable parasitic nematodes to target humans and provide the foundation for drug development to prevent human infection.

eTOC Blurb

Bryant *et al*. report that the skin-penetrating, human-parasitic nematode *Strongyloides stercoralis* relies on a conserved thermosensory neuron pair to drive attraction to human body heat. The

*Corresponding author: ehallem@ucla.edu.

†Present address: Molecular & Cellular Biology in Seattle Program, Fred Hutchinson Cancer Research Center, 1100 Fairview Ave N, Seattle, WA 98115

‡Present address: Yale Interdepartmental Neuroscience Program, Yale University, 260 Whitney Ave, New Haven, CT 06511

Author Contributions

A.S.B. and E.A.H. conceived the study and wrote the manuscript. A.S.B., F.R., and J.L. performed all experiments and analyzed the data. All authors read and approved the final manuscript.

Declaration of Interests

The authors declare no competing interests.

Inclusion and Diversity

One or more of the authors of this paper self-identifies as a member of the LGBTQ+ community. One or more of the authors of this paper received support from a program designed to increase minority representation in science.

authors demonstrate that parasite-specific sensory encoding strategies drive temperature-driven host seeking by human-infective parasitic worms.

Keywords

parasitic nematode; parasitic helminth; host seeking; thermosensation; thermotaxis; *Strongyloides stercoralis*

Introduction

Soil-transmitted gastrointestinal helminths are a major source of neglected disease affecting the world's most socioeconomically depressed communities[1–8]. Although the prevalence of parasitic helminth infections is highest in developing nations, infections persist within impoverished areas of developed nations, including the United States[4,5]. Infection with soil-transmitted gastrointestinal helminths causes chronic gastrointestinal distress as well as stunted growth and cognitive impairment in children. Current therapeutics against parasitic nematodes exclusively target ongoing infections. These anthelmintic drugs have variable efficacy at clearing infections, and the lack of prophylactic treatments results in high reinfection rates[9–12]. Additionally, repeated dosage with anthelmintics may give rise to drug-resistant parasites[9–11], underscoring the need for preventative strategies. A mechanistic understanding of how parasitic nematodes locate human hosts will enable the development of new therapeutic approaches to preventing infections.

The skin-penetrating human threadworm *Strongyloides stercoralis* is a human-parasitic gastrointestinal helminth that is estimated to infect at least 610 million people worldwide, nearly three times as many people as malaria[13]. Infections with *S. stercoralis* are of particular concern because these infections are often fatal for immunosuppressed individuals, a fact that bears additional urgency given that front-line immunosuppressive treatments in the current COVID-19 pandemic exacerbate the risk that latent infections will erupt into acutely fatal disease[14–16]. Like other skin-penetrating nematodes, *S. stercoralis* infects hosts exclusively as developmentally arrested third-stage infective larvae (iL3s). The iL3s are soil-dwelling and actively locate hosts using host-emitted sensory cues (Figure 1A)[17,18]. They then infect hosts by penetrating directly through the skin of the feet or other exposed skin.

Host detection and subsequent infection require thermal cues[18,19]. *S. stercoralis* iL3s display robust attraction to human body heat when exposed to temperatures above an ambient cultivation temperature (T_C; Figure 1B)[18]. Moreover, the preference of iL3s for body heat is thought to act as a major driver of long-range navigation toward hosts[20]. This heat-seeking behavior is specific to mammalian-parasitic nematodes: insect-parasitic nematodes and the free-living model nematode *Caenorhabditis elegans* are not attracted to mammalian body heat[18]. Indeed, for *C. elegans*, exposure to temperatures above T_C drives either negative thermotaxis, or noxious heat avoidance when the temperature is above *C. elegans'* 15–25°C physiological temperature range[21–26].

Although the molecular and neural basis of *C. elegans* thermosensation has been extensively studied[21,24,26,27], the mechanisms that underlie the very different thermosensory behaviors of parasitic nematodes are unknown. Many of the same neurons are present in *S. stercoralis* and *C. elegans*[17], leading to the fundamental question of how these anatomically similar nervous systems generate drastically different behavioral repertoires. This question was not feasible to address previously due to the lack of a genetic toolkit for interrogating neural function in parasitic nematodes.

Here, we identify cellular and molecular specializations that drive heat seeking in parasitic nematodes. We identify and characterize the primary thermosensory neurons in *S. stercoralis* by applying single-cell genetic targeting, cell-type-specific neural silencing, and fluorescent biosensor techniques for the first time in any non-*Caenorhabditis* nematode. We show that the thermosensory neurons of a human parasite are specialized for the precise encoding of temperatures up to human body heat, enabling these parasites to robustly track human hosts. These neurons are sensitive to thermal experience in a manner that supports the ability of iL3s to adjust their heat-seeking behaviors in response to altered environmental conditions. In addition, rapid sensory adaptation enables *S. stercoralis* iL3s to behaviorally differentiate between host and sub-host heat sources. Thermosensory proteins tuned for human body heat generate the expanded responsiveness of parasite thermosensory neurons relative to homologous neurons in *C. elegans*. Our results pinpoint the specific cellular and molecular adaptations that enable endoparasitic animals to target human hosts.

Results

Genetic identification of *S. stercoralis* thermosensory neurons

To understand the neural mechanisms of thermosensation in *S. stercoralis* iL3s, we first used a genetic approach to identify the primary thermosensory neurons. This approach resolved the historical challenge of identifying *S. stercoralis* thermosensory neurons, which arose from species-specific morphological differences in sensory neuron dendritic structure that complicated anatomical comparisons across species[20]. In *C. elegans*, the AFD sensory neuron pair provides the primary thermosensory drive for thermotaxis navigation toward a remembered cultivation temperature[26,28–31]. *C. elegans* AFD neurons are structurally defined by “finger-like” microvilli that emerge from the dendritic ends at the nose of the animal and are thought to enhance neuronal sensitivity to temperature fluctuations[26]. *S. stercoralis* lacks sensory neurons with these “finger-like” structures[20,32]. The closest anatomical homologs appear to be the multi-layered “lamellae” of the ALD neurons, which are the only elaborate sensory endings in the *S. stercoralis* amphid sensory organs[32]. However, due to both variations in the arrangement of the cell bodies that comprise the amphid sensory organs and life-stage-specific changes in the morphology of sensory neurons, whether ALD neurons are homologs of the *C. elegans* AFD thermosensory neurons or AWC chemosensory neurons (the other *C. elegans* amphid neurons with elaborate sensory endings) was unclear[20,32–34].

In *C. elegans*, the receptor-type guanylate cyclases (rGCs) GCY-8, GCY-18, and GCY-23 are expressed selectively in *C. elegans* AFD, contribute to thermosensation via activation of the cyclic GMP-gated cation channels composed of TAX-2 and TAX-4 subunits, and are used

as AFD-specific genetic markers[31,35–38]. The *S. stercoralis* TAX-4 homolog, *Ss*-TAX-4, is required for positive thermotaxis by iL3s[18]. Thus, parasite homologs of the AFD-specific rGCs may serve as molecular markers for AFD-specific function, permitting the genetic identification of the sensory neurons that drive the thermotaxis behaviors of *S. stercoralis* iL3s.

The *C. elegans* genome contains an unusually large number of receptor-type guanylate cyclases compared with mammalian genomes[39,40]. To assess whether this gene family is similarly expanded in *Strongyloides* species, we used TBLASTN to catalogue orthologs of the 26 *C. elegans* rGC proteins (Data S1) in *S. stercoralis* and the closely related rat parasite *Strongyloides ratti*. After identifying *S. stercoralis* and *S. ratti* genomic regions with potential homology to members of the *C. elegans* rGC gene family, we performed manual curation of overlapping gene models retrieved from WormBase ParaSite (WBPS16; Data S1 and Table S1). We found that, like *C. elegans*, the genomes of *S. stercoralis* and *S. ratti* contain large numbers of rGCs – our manual curation pipeline revealed at least 24 fully sequenced rGC genes for *S. stercoralis* and 23 for *S. ratti*. Our TBLASTN search identified three additional *S. stercoralis* genomic loci containing sequences encoding guanylate cyclase protein features (*e.g.*, guanylate cyclase domain, transmembrane domain). However, these matches localize to partial contig fragments; since full sequences for the overlapping genes (SSTP_0000270000, SSTP_0000334600, SSTP_000962000; Data S1) are not available, we excluded these potential rGCs from further analysis.

Next, we performed a phylogenetic comparison between the updated rGC protein sequences for *S. stercoralis*, *S. ratti*, and *C. elegans* (Figure S1). This analysis revealed that although all three species contain approximately the same number of rGC genes, the degree of direct homology varies. For some rGCs, including *C. elegans daf-11* and *gcy-9*, we identified putative 1-to-1 homologs in each *Strongyloides* genome. However, the majority of *C. elegans* rGCs are not clearly homologous to individual *Strongyloides* genes, and vice versa. In contrast, most *S. stercoralis* rGCs have clear 1-to-1 homolog matches to *S. ratti* genes, mirroring previous phylogenetic comparisons of rGCs in *C. elegans* and *Caenorhabditis briggsae*[39,40].

To enable cell-type-specific labeling of AFD neurons in parasites, we next sought to identify parasite homologs of rGCs that are selectively expressed in *C. elegans* AFD (AFD-rGCs). Our phylogenetic analysis revealed that the genomes of *S. stercoralis* and *S. ratti* each contain three putative AFD-rGCs. The pattern of clear within-genus homologs paired with indirect homology between *Strongyloides* and *Caenorhabditis* is present for the AFD-rGCs. Although there is clear 1-to-1 homology between the *Strongyloides* species, all six *Strongyloides* sequences are most homologous to *C. elegans* GCY-23 (Figure 1C, Figure S1). Receptor-type guanylate cyclase proteins contain distinct domains, including a 5’ extracellular domain, a transmembrane domain, and a 3’ intracellular domain comprised of a kinase homology domain and a cyclase domain (Figure S1B). Protein sequence homology between *Strongyloides* and *C. elegans* sequences is lowest in the extracellular domain and highest in the guanylate cyclase domain; despite differences in the degree of homology across topographical and functional domains, *Ce*-GCY-23 is consistently the closest match for *Strongyloides* sequences, as for the full-length protein (Figure S1C).

Based on protein sequence homology, we therefore named the *S. stercoralis* and *S. ratti* homologs GCY-23.1, GCY-23.2, and GCY-23.3. We then extracted promoter sequences for the three *S. stercoralis* rGCs, as well as *Sr*-GCY-23.2, and found that all four promoters drive strong transgene expression in a single TAX-4-positive head neuron pair in *S. stercoralis* iL3s (Figure 1D, Figure S2). Using confocal microscopy, we found that this neuron pair displays elaborate structures at the nose tip that strongly resemble electron microscopy reconstructions of the ALD lamellae (Figure 1D)[33,34]. Based on genetic homology, we thus identified the *S. stercoralis* ALD neurons as homologs of the *C. elegans* AFD neurons (and hereafter refer to them as *S. stercoralis* AFD neurons, or *Ss*-AFD).

S. stercoralis AFD neurons are required for heat seeking

To test whether the *Ss*-AFD neurons are required for the attraction of *S. stercoralis* iL3s to mammalian body heat, we chemogenetically silenced them via AFD-specific expression of the *Drosophila* histamine-gated chloride channel HisCl1[41], which we codon-optimized for *Strongyloides* (Figure S3A). We found that silencing *Ss*-AFD reduced the migration of iL3s toward temperatures approximating mammalian body heat (Figure 1E). Exposure to warm temperatures between ambient and host body temperature is known to increase the movement speed of *S. stercoralis* iL3s and promote a switch from highly curved local search behaviors to relatively straight long-distance navigation[18]. *Ss*-AFD is required for these temperature-dependent changes in behavior: AFD-silenced iL3s moved slower and more circuitously in the thermal gradient than control iL3s (Figure 1E). In fact, the movement of AFD-silenced iL3s was similar to that of wild-type iL3s migrating in an isothermal room temperature environment (Figure S3B). We validated that activation of *Ss*-AFD-expressed HisCl1 channels muted thermosensory responses in those neurons, via calcium imaging (see below, Figure S3C, D). Our results establish single-neuron genetic targeting for the first time in any non-*Caenorhabditis* nematode and demonstrate that the *Ss*-AFD neurons are required for the heat-seeking behavior of iL3s, thus confirming the impact of *Ss*-ALD laser ablation[33].

Novel encoding of warming stimuli by *S. stercoralis* AFD neurons

Do temperature-driven responses in *Ss*-AFD display species-specific adaptations, or is AFD encoding of temperature conserved between parasitic and free-living nematodes? We generated iL3s expressing yellow cameleon YC3.60[42] in *Ss*-AFD, which allowed us to image neural activity for the first time in any non-*Caenorhabditis* nematode. We designed thermal stimuli that mimic the temperatures experienced by iL3s engaged in positive thermotaxis toward host body temperatures; these warming stimuli were delivered to immobilized worms via a custom PID-controlled thermal stimulator (warming rate = 0.025 °C/s; Figure S4A, B). We then imaged from *S. stercoralis* AFD and *C. elegans* AFD under the same experimental conditions. Consistent with previous findings[26,36,43,44], warming stimuli drove large depolarizations in *C. elegans* AFD (*Ce*-AFD) above a response threshold (T^*_{AFD}) set near the recently experienced ambient temperature (Figure 2A, B). *Ce*-AFD monotonically and nonlinearly encoded temperature deviations near the ambient temperature, such that the lowest *Ce*-AFD response was the baseline response driven by the coldest temperature in the thermal stimulus (T_0, 20°C; Figure 2C) and the *Ce*-AFD response

was positively correlated with increasing temperature only in a narrow temperature range near T^*_{AFD} (Figure 2D–H).

In contrast, temperature-driven responses in *Ss*-AFD encoded different features of the thermal stimulus and displayed multiple parasite-specific adaptations. *Ss*-AFD also had a response threshold near the ambient temperature (Figure 2A, B). However, the *Ss*-AFD response at T^*_{AFD} was dominated by a warming-triggered inhibition, such that the *Ss*-AFD responses were reduced below the baseline T_0 (20°C) response. We quantified this effect by calculating the temperature that drove the lowest *Ss*-AFD response, where "lowest" is defined as less than or equal to the response at 20°C. Unlike *Ce*-AFD, the temperature that elicited the lowest *Ss*-AFD response was usually above 20°C, closer to the ambient temperature (Figure 2C). This warming-triggered inhibition resulted in a negative monotonic relationship between temperature and *Ss*-AFD activity near ambient (Figure 2D, E). Following warming-triggered inhibition, *Ss*-AFD responses showed near-linear positive encoding of temperatures ranging from near ambient to above human body temperature, with peak excitatory responses driven by the warmest temperature in the stimulus (Figure 2F–H, Figure S5). Thus, *Ss*-AFD utilizes both nonlinear and near-linear encoding of temperature information. We speculate that the initial reduction in neural activity, achieved via warming-triggered inhibition, effectively "resets" the dynamic range of *Ss*-AFD, expanding the range of above-ambient temperatures that can be differentially encoded. A parasite-specific encoding strategy that combines a threshold nonlinearity with near-linear encoding of temperatures up to host body heat likely enables *Ss*-AFD to maximize both thermal sensitivity and the information conveyed in physiologically relevant temperature ranges. The relative abilities of *Ce*-AFD adults and *Ss*-AFD iL3s to encode temperatures near body heat align with the distinct physiological temperature ranges of these two species/life stages. Notably, given the importance of heat seeking for host targeting by iL3s, the presence of parasite-specific mechanisms that sculpt the unique *Ss*-AFD thermosensory responses highlights the potential for elements in the *S. stercoralis* thermotransduction pathway to serve as novel targets for parasite-specific therapeutic interventions.

Ss-AFD responses are regulated by temperature experience

The thermotaxis behaviors of both *S. stercoralis* and *C. elegans* are regulated by thermal experience[20,26,45]. In *C. elegans*, AFD thermal thresholds are determined by the just-experienced ambient temperature (*i.e.,* the holding temperature), which often coincides with the animal's cultivation temperature[26,36,43–45]. To determine whether responses in *Ss*-AFD display experience-dependent changes in thermosensitivity, we tested the impact of shifting the cultivation and holding temperatures together. We cultivated worms overnight at 15°C, then exposed them to warming temperature ramps that were shifted toward cooler temperatures, such that the starting temperature in the stimulus (*i.e.,* the holding temperature) was also 15°C; we refer to the combined cultivation and holding temperature as $T_{ambient}$ (Figure S4C). Exposure to a $T_{ambient}$ of 15°C shifted T^*_{AFD} toward cooler temperatures in both *Ss*-AFD and *Ce*-AFD (Figure 3A–D). The downward shift in thermal threshold did not eliminate the unique properties of the *Ss*-AFD response. The response at the cooler T^*_{AFD} was still dominated by warming-triggered inhibition, with a peak hyperpolarization just above T^*_{AFD} (Figure 3E), and a peak depolarization

in response to the warmest temperature in the stimulus (Figure 3F). Notably, despite the shift in T^*_{AFD} toward cooler temperatures, *Ss*-AFD still responded near-linearly to temperatures up to host body temperatures (Figure 3C), consistent with earlier behavioral results demonstrating that *S. stercoralis* iL3s cultivated at 15°C engage in robust positive thermotaxis toward skin temperatures[18]. The preservation of near-linear encoding at host body temperatures, combined with experience-dependent expansions in the dynamic range of *Ss*-AFD thermosensitivity, further supports a model in which parasite-specific adaptations in sensory information processing pathways actuate the ability of iL3s to host seek across a range of ethological contexts.

S. stercoralis iL3s migrate toward cool temperatures

Besides attraction to host body temperatures, mammalian-parasitic iL3s display negative thermotaxis: migration toward cooler temperatures when exposed to temperatures below their ambient cultivation temperature[18]. Previously, negative thermotaxis was measured exclusively using iL3s exposed to a ~20–34°C gradient[18]. To investigate how iL3s behave in thermal gradients at lower temperatures, we measured migration in a ~12–22°C gradient (Figure S6). When placed at 20°C or 17°C, iL3s cultivated at 23°C displayed negative thermotaxis, accumulating near ~16°C (Figure S6A). These migration patterns are regulated by recent experience, such that iL3s cultivated at 15°C for at least 2 hours accumulated at cooler temperatures than iL3s cultivated at 23°C (Figure S6B–D). In contrast, iL3s placed at 14°C in a ~12–22°C gradient remained at cooler temperatures, regardless of cultivation temperature (Figure S6). These results suggest that negative thermotaxis by *S. stercoralis* iL3s is regulated by the strength of thermal drive, which decays as a function of deviations from T_C, similar to positive thermotaxis[18].

Ss-AFD mediates negative thermotaxis via an *Ss-tax-4* signaling cascade

Positive and negative thermotaxis behaviors represent distinct iL3 behavioral modes, raising the question of whether these behaviors are regulated by the same signaling cascades and primary sensory neurons. We found that CRISPR/Cas9-mediated targeted mutagenesis of *Ss-tax-4*[46] and HisCl1-mediated silencing of *Ss*-AFD activity both abolished negative thermotaxis by iL3s (Figure 4A, B), similar to positive thermotaxis (Figure 1E)[18]. In *C. elegans*, positive and negative thermotaxis behaviors toward T_C also rely on *Ce-tax-4*-dependent sensory transduction in *Ce*-AFD[26,36,47,48]. Thus, our results provide additional evidence that the opposing thermosensory behaviors of *S. stercoralis* iL3s and *C. elegans* adults reflect adaptations of a broadly conserved nematode thermosensory circuit.

Next, we tested the effect of cooling temperature ramps on *Ss*-AFD activity, compared to *Ce*-AFD (Figure 4C, D). Although *Ce*-AFD responses were reduced during a rapidly cooling temperature ramp (range: 22–13°C, Figure 4D), simple linear regression analysis found that *Ce*-AFD response magnitudes were significantly predicted by recording time (Figure 4E; regression equation: $Y = -0.021*X + 3.59$, $R^2 = 0.70$; replicates test for lack of fit: discrepancy (F) = 1.96, $p = 0.17$), across timepoints where the change in temperature was non-linear (Figure 4F). This result raises the possibility that the reductions we observe in *Ce*-AFD under our specific experimental conditions may be due to photobleaching. In contrast to our *Ce*-AFD responses, reductions in the *Ss*-AFD responses were not fully

predicted by recording time (Figure 4D–F; regression equation: $Y = -0.041*X + 6.60$, $R^2 = 0.61$; replicates test for lack of fit: discrepancy (F) = 4.56, $p < 0.05$). Previous studies using electrophysiology have measured cooling-activated hyperpolarizations in *Ce*-AFD[36], suggesting that the lack of clear responses in our experiments may be due to the difficulty of resolving decreases in already-low activity rates using calcium indicators. If true, this explanation further suggests that our ability to measure cooling-activated decreases in *Ss*-AFD could be because *Ss*-AFD has higher tonic activity levels than *Ce*-AFD. This interpretation aligns with our observation of warming-triggered inhibition in *Ss*-AFD, which indicates that baseline *Ss*-AFD activity is high enough to reveal negative deviations via calcium imaging.

It remains unclear how changes in AFD activity are translated into the robust behaviors of *S. stercoralis* iL3s in cool temperature gradients. Taken together, our results, particularly the lack of major species-specific differences in the direction of neural responses associated with cool temperatures, suggest that the mechanisms that sculpt the different behavioral responses of free-living and parasitic nematodes to below-ambient temperatures are downstream of AFD.

S. stercoralis iL3s display a unique "U-turn" behavior at temperatures below host body temperature

When navigating in the environment, *S. stercoralis* iL3s likely encounter temperature gradients that terminate well below host body temperature and do not directly reflect the presence of a host animal (*e.g.,* sun-warmed soil or recently deposited fecal piles). Do iL3s have a mechanism that enables them to avoid accumulation at these "false positive" heat sources? To address this question, we examined the behavior of iL3s in temperature gradients that are warmer than ambient but well below host body heat. We first exposed iL3s cultivated at 23°C to temperature gradients ranging from 15–25°C (T_{start} = 23°C). Under these conditions, most iL3s initially engaged in positive thermotaxis and accumulated at the warmest temperature in the gradient, consistent with the behaviors of iL3s in thermal gradients that end near host body temperature[18]. However, unlike our observations with warmer gradients, we found that within minutes some of these heat-seeking iL3s seemingly reversed their thermal preferences, transitioning to sustained negative thermotaxis (Figure 5A; median percent of heat-seeking iL3s that reversed their thermal preference = 35%; median dwell time near maximum temperature reached = 216 s). This behavior, in which iL3s essentially perform a "U-turn" in the thermal gradient, is distinct from the stereotyped reversal maneuvers employed by *C. elegans*, which feature backward movement of the entire animal[49]. U-turns could occur before worms reached the edge of the agar surface, suggesting that this reversal of thermal preferences is not driven by physical interactions. U-turns also do not appear to result from a lack of explorable area: iL3s that did not perform U-turns (often the majority of the population) continued to explore the vertical axis of the plate after reaching the warmest temperature. However, we cannot exclude the possibility that additional sensory signals contribute to this behavior.

Worms cultivated at 15°C displayed similar U-turn behaviors (Figure 5B; median dwell time near maximum temperature reached = 126 s), with increased frequencies observed in

thermal gradients that terminate closer to T_C (Figure 5C; median percent of heat-seeking iL3s that U-turned in a 15–25°C gradient = 3.46%, median percent of heat-seeking iL3s that U-turned in a 12–22°C gradient = 97.25%). Across cultivation temperatures, U-turns were only observed in thermal gradients that ended well below host body temperature. Thus, the likelihood that iL3s will abruptly switch the valence of their thermal preferences is modulated by both cultivation temperature and the assay gradient (Figure 5C).

To test for neural correlates of the U-turn behavior, we designed imaging stimuli that mimicked U-turn trajectories (Figure 5D), then quantified *Ss*-AFD responses at the transition between an initial warming ramp and sustained "steady-state" exposure to a temperature stimulus. We found that *Ss*-AFD steady-state responses rapidly (within ~60 s) adapted toward the ambient temperature response (Figure 5E–H). To test whether this rapid adaptation may be a neural correlate of the U-turn transition from positive to negative thermotaxis, we compared *Ss*-AFD responses to a range of maximum temperatures associated with a range of U-turn rates across the population: 22°C (many worms U-turn), 26°C (some worms U-turn) and 32°C (no worms U-turn). We found that the degree of *Ss*-AFD response adaptation approximated the likelihood that thermal stimuli would drive positive-to-negative thermotaxis U-turns: when $T_{ambient}$ was 15°C, *Ss*-AFD responses to steady-state thermal stimuli strongly adapted at 22°C, moderately adapted at 26°C, and did not adapt at 32°C (Figure 5F–H). This result suggests that rapid adaptation in the *Ss*-AFD response to some, but not all, temperature stimuli may underlie the ability of iL3s to abruptly abandon positive thermotaxis in favor of sustained negative thermotaxis.

The *Ss*-AFD responses that displayed the greatest steady-stage adaptation (Figure 5F, G) were in response to steady-state stimulation at 22°C; at this temperature, *Ss*-AFD is usually hyperpolarized due to the warming-triggered inhibition. We tested whether this rapid adaptation reflects a general inability of *Ss*-AFD to maintain prolonged hyperpolarization. Cooling temperature ramps from 22–13°C drove *Ss*-AFD hyperpolarizations of similar magnitude to non-adapted warming-triggered hyperpolarizations at 22°C, but did not display rapid adaptation (Figure 5I, J). These results suggest that *Ss*-AFD response adaptation is likely a consequence of the thermal stimuli themselves rather than the direction of the *Ss*-AFD response, and that distinct processes drive cooling- and warming-triggered hyperpolarizations in *Ss*-AFD.

The *Ss*-AFD-rGCs each confer sensitivity to temperature ranges spanning ambient and host body heat

Next, we sought to identify molecular mechanisms that underlie the expanded responsiveness of *Ss*-AFD to mammalian body temperatures. In *C. elegans*, the AFD-specific rGCs are required for thermosensory activity in AFD[31,35,36]. These proteins localize exclusively to the elaborate finger-like processes of *Ce*-AFD[37,50]. Given the unique lamellar structure of the *S. stercoralis* AFD sensory ending (Figure 1D), we first tested the intracellular localization of *Ss*-AFD-rGCs. A GFP-tagged version of *Ss*-GCY-23.1 localized to the distal end of the *Ss*-AFD process (Figure 6A). Intriguingly, *Ss*-GCY-23.1 intracellular localization is restricted to the most elaborate anterior end of the *Ss*-AFD process (Figure 6B). A more posterior section of the *Ss*-AFD process that displays reduced, but still present,

lateral complexity does not contain *Ss*-GCY.23.1 expression. The functional relevance of these apparent intracellular domains within the elaborate lamellar structure of *Ss*-AFD is not clear, although we speculate this division acts to partition cGMP signaling machinery, similar to the bipartite signaling compartment of *Ce*-AFD[50].

Misexpression of *Ce*-GCY-18 and *Ce*-GCY-23, but not *Ce*-GCY-8, can confer TAX-4-dependent sensitivity to thermal stimuli (Figure S7A)[35]. To determine whether the *S. stercoralis* AFD-rGCs (*Ss*-GCY-23.1, *Ss*-GCY-23.2, and *Ss*-GCY-23.3) have thermosensory capabilities similar to *Ce*-GCY-23, we ectopically expressed each *Ss*-AFD-rGC in *C. elegans* ASE chemosensory neurons also expressing the YC3.60 calcium sensor, then measured responses to warming temperature ramps. *Ce*-ASE was chosen as the ectopic expression site, rather than *Ce*-AFD, in order to examine the thermosensory properties of the *Ss*-AFD-rGCs independent of mechanisms for *Ce*-AFD-specific signal amplification[26,35]. *Ce*-ASER is activated by cooling, with an activation threshold of ~18°C[51]. We first measured baseline activity of *Ce*-ASE neurons to our 20–40°C warming temperature ramp. We did not observe increased activity upon cooling or decreases in activity following warming (Figure S7B), confirming that *Ce*-ASE does not display significant thermosensory responses above its activation threshold.

In contrast to the wild-type responses of *Ce*-ASE neurons, we found that ectopic expression of each *S. stercoralis* AFD-rGC conferred thermosensitivity to above-ambient temperatures. The functional properties of all three of the *Ss*-AFD-rGCs differed from each other and from those of the *C. elegans* AFD-rGCs (Figure 6C, D, Figure S7). For *Ss*-GCY-23.1 and *Ss*-GCY-23.3 ectopic expression, the threshold of temperature-evoked activity (T^*_{ASE}, defined based on significant, sustained deviation from baseline *Ce*-ASE responses) was near mammalian skin temperature; *Ss*-GCY-23.2 expression resulted in thermosensory activity with a T^*_{ASE} near ambient temperature (Figure 6D).

Notably, all three *Ss*-AFD-rGCs conferred thermosensitivity up to host body temperatures. Across the *Ss*-AFD-rGCs, the temperature driving maximal responses varied such that *Ss*-GCY-23.3 responses peaked at warmer temperatures than *Ss*-GCY-23.1 and *Ss*-GCY-23.2 (Figure 6D). These results suggest that changes in the functional properties of *Ss*-AFD-rGCs, including an expanded responsiveness to mammalian body temperatures relative to *C. elegans* homologs, contribute to both the parasite-specific encoding of thermal cues in *Ss*-AFD and the preference of *S. stercoralis* iL3s for mammalian body heat.

Warming-triggered inhibition in *Ss*-AFD reflects a reduction in cyclic GMP

Ss-AFD calcium responses display a pronounced warming-triggered inhibition (Figure 2A) that is not reflected in the temperature-evoked calcium activity observed following ectopic expression of *Ss*-AFD-rGCs in *Ce*-ASE (Figure 6C). This observation suggests that initial reductions in *Ss*-AFD activity following exposure to near-ambient warming temperatures are likely not an intrinsic property of the *Ss*-AFD-rGC thermoreceptors. We sought to identify whether warming-triggered inhibition in the *Ss*-AFD calcium response reflects a reduction of cGMP levels, which would lead to a reduction in cGMP-gated channel activity and thus a decreased calcium signal. We generated iL3s expressing the cGMP sensor FlincG3[52,53] in *Ss*-AFD, and measured cGMP levels in response to a warming stimulus centered on the

ambient temperature (ramp: 20–25°C at 0.025 °C/s). At the *Ss*-AFD sensory tips, exposure to near-ambient warming temperatures resulted in a significant decrease in cGMP levels (Figure 7A). The response threshold (the temperature at which FlincG3 signals deviated significantly from the baseline response at 20°C) was similar to the response thresholds for *Ss*-AFD calcium responses, suggesting that the warming-triggered inhibition observed via YC3.60 imaging is due to a temperature-dependent decrease in cGMP. During steady-state application of an above-ambient temperature (25°C), reduced cGMP levels partially adapted back toward the response at ambient temperatures (Figure 7A). This observation suggests that the rapid adaptation in *Ss*-AFD calcium responses associated with thermotaxis U-turn behaviors (Figure 5) reflects, at least in part, cGMP response dynamics. The molecular mechanisms that produce temperature-dependent reductions in cGMP levels in *Ss*-AFD are not yet known but may involve cGMP hydrolysis via cGMP-selective phosphodiesterase activity. In *C. elegans*, temperature-dependent regulation of cGMP hydrolysis may help shape the threshold and temporal dynamics of thermal responses[26,38]. Future experiments are needed to test whether *S. stercoralis* phosphodiesterases display parasite-specific thermal sensitivities that help generate the unique features of thermosensory encoding in *Ss*-AFD neurons, as well as the impact of these encoding features on the thermal behaviors of parasites.

Discussion

Here, we identify multiple parasite-specific molecular, cellular, and behavioral adaptations in the thermosensory circuit of the human parasite *S. stercoralis* that enable it to locate human hosts. We present the first uses of single-cell genetic targeting and neural imaging methods in any endoparasitic animal, as well as the first demonstration of parasite-specific sensory encoding strategies that underlie host seeking by soil-transmitted parasitic helminths. We show that free-living and parasitic nematodes rely on a homologous thermosensory neuron pair, named AFD, to drive their divergent thermal preferences and behaviors. We find that *S. stercoralis* AFD neurons display temperature-driven activation properties distinct from those observed in the free-living model *C. elegans*, including both nonlinear and near-linear encoding of temperatures from below ambient to human body heat. These unique, parasite-specific response properties provide a mechanism for *Ss*-AFD to encode additional information and differentiate between a broad range of host and environmental temperatures, and are likely critical for the ability of iL3s to host seek over relatively long distances[17].

Nematode nervous systems are remarkably well conserved, to the extent that many of the same neurons are found across free-living and parasitic species[17,54–56]. Despite a high degree of anatomical conservation, different species have strikingly divergent lifestyles and behavioral repertoires. For example, *C. elegans* is a free-living bacterivore whose natural habitat is decaying organic matter such as rotting fruit[57], while *S. stercoralis* is a human-infective worm that inhabits the soil as an infective larva and the human gut as a parasitic adult[58]. How such anatomically similar nervous systems can support species-specific ethological requirements has remained an unanswered question. Our results demonstrate that the parasite-specific behaviors of soil-transmitted nematodes emerge from

functional adaptations at the earliest stages of sensory information processing and are driven in part by differences in the tuning properties of the thermoreceptor proteins.

The behavioral strategies that guide parasitic nematodes to human hosts are not fully understood. Here, we report a new behavioral component of temperature-driven host seeking: the ability to rapidly reverse erroneous attraction to non-host heat sources. This novel behavior appears to be generated by rapid sensory adaptation selectively triggered by exposure to sub-body-heat temperatures. In *C. elegans*, although *Ce*-AFD can display minutes-long adaptation to recent temperature experiences[26,36,45,59], these changes do not appear to affect behavioral temperature preferences, which are thought to adapt primarily on longer (hours-long) timescales[21,26,45,60]. Thus, the ability of iL3s to engage in thermotaxis "U-turns", rapidly transitioning from sustained positive thermotaxis to sustained negative thermotaxis, may reflect a parasite-specific behavioral consequence of sensory adaptation that permits iL3s to quickly adjust their host-seeking behaviors after encountering a non-host heat source. We also show that exposure to new environmental temperatures triggers changes in the dynamic range of *Ss*-AFD thermosensitivity while preserving the ability to encode host body heat. Together, these results suggest that soil-transmitted nematodes utilize a host-seeking strategy that both relies on the precise encoding of temperature to direct worms toward host animals over long distances and flexibly adjusts in response to sensory experience.

Here, we demonstrate that the cellular mechanisms of thermal encoding are fundamentally different in *S. stercoralis* and *C. elegans*. Historically, most research on parasitic nematodes has used the free-living nematode *C. elegans* as a genetically tractable model for human parasites. Our data indicate that this approach is not sufficient given the dramatically different neural mechanisms that operate in the two species and emphasize the essential role of mechanistic studies in parasitic nematodes themselves for understanding the neural basis of parasitism in these species. Parasitic nematode infections are one of the world's most neglected sources of chronic disease and economic burden. Our finding that the sensory neurons of parasitic nematodes display parasite-specific functional adaptations identifies parasite sensory neurons as promising targets for anthelmintic control strategies.

STAR Methods

RESOURCE AVAILABILITY

Lead Contact—Further information and requests for resources and reagents should be directed to and will be fulfilled by the Lead Contact, Dr. Elissa Hallem (ehallem@ucla.edu).

Materials Availability—All unique reagents generated in this study are available from the Lead Contact.

Data and Code Availability

- The data that support the findings of this study have been deposited at Zenodo and are publicly available as of the date of publication. DOIs are listed in the key resources table.

- All original code has been deposited at Zenodo and is publicly available as of the date of publication. DOIs are listed in the key resources table.
- Any additional information required to reanalyze the data reported in this paper is available from the lead contact upon request.

EXPERIMENTAL MODEL AND SUBJECT DETAILS

All protocols and procedures involving vertebrate animals were approved by the UCLA Office of Animal Research Oversight (Protocol ARC-2011-060), which adheres to the standards of the AAALAC and the *Guide for the Care and Use of Laboratory Animals*.

Maintenance of *Strongyloides stercoralis*—*S. stercoralis* UPD strain (originally provided by Dr. James Lok, University of Pennsylvania) was maintained as previously described[18]. Briefly, *S. stercoralis* was serially passaged through male Mongolian gerbils (Charles River Laboratories) and maintained on fecal-charcoal plates. Gerbils were placed under isoflurane anesthesia before receiving ~2,250 iL3s in 200 μL of sterile PBS via inguinal subcutaneous injections. Feces infested with *S. stercoralis* were collected by placing infected gerbils on wire cage racks overnight with damp cardboard liners on the cage bottoms. The following morning, fecal pellets were collected, mixed in a 1:1 ratio with autoclaved charcoal granules, and stored in 10-cm-diameter Petri dishes lined with wet 10-cm-diameter Whatman filter paper. Feces containing *S. stercoralis* were collected for 14–45 days post-inoculation. Fecal charcoal plates were initially stored for 48 hours at 20°C, then either used for microinjection (free-living adults) or moved to a 23°C incubator for an additional 6–14 days until use in behavioral assays (iL3s). *S. stercoralis* free-living adults and iL3s were collected from fecal-charcoal plates via a Baermann apparatus[63].

Transgenic *S. stercoralis* F_1 iL3s were generated by microinjection of plasmid constructs into free-living adult females using standard methods[64], with modifications as previously described[19]. Fecal-charcoal plates containing microinjected females and wild-type adult males were incubated at 23°C for a minimum of 5 days prior to screening and experimental use. To generate transgenic F_1 iL3s expressing fluorescent reporters, plasmids (including: pJHL09, pASB25, pASB41, pASB42, pASB51, and pMLC41[18]) were microinjected at 40–100 ng/μL. A full list of all plasmids used in this study are provided in Table S2. Targeted mutagenesis of *Ss-tax-4* was accomplished using established *Strongyloides* CRISPR/Cas9 protocols[18,46], with the following modifications. For generating *Ss-tax-4* iL3s, injection mixes contained 80 ng/μL pMLC47, 80 ng/μL pEY11, and 40 ng/μL pPV540. For generating no-Cas9 controls, injection mixes contained 80 ng/μL pMLC47 and 80 ng/μL pEY11. For calcium imaging of *S. stercoralis* AFD, *Sr-gcy-23.2p::strYC3.60* F_1 iL3s were generated by microinjecting pASB52 at a concentration of 80 ng/μL. For generating *Sr-gcy-23.2p::strHisCl1* iL3s, injection mixes contained 80 or 100 ng/μL pASB30 with 50 ng/μL pJHL09 as a co-injection marker. For calcium imaging of HisCl1-silenced *Ss*-AFD neurons, *Sr-gcy-23.2p::strHisCl1::P2A::mRFPmars; Sr-gcy-23.2p::strYC3.60* F_1 iL3s were generated by co-injecting pASB56 and pASB52, both at 80 ng/μL. For generating *Sr-gcy-23.2p::strFlincG3* iL3s, injection mixes contained 80 ng/μL pASB67.

Maintenance of *C. elegans*—*C. elegans* adults were raised on 2% Nematode Growth Media (NGM) plates seeded with a lawn of *Escherichia coli* OP50 bacteria, as per standard methods[65]. *C. elegans* experiments exclusively used young adult hermaphrodites; adult males were used only for crosses. Calcium imaging of *C. elegans* AFD was performed using strain IK890 *njEx358[gcy-8::YC3.60, ges-1::NLS-tagRFP]*, which was obtained from Dr. Ikue Mori (Nagoya University). Calcium imaging of *C. elegans* ASE was performed using strain XL115 *lin-15(n765) ntIs14[flp-6::YC3.60; lin-15+]*, which was obtained from Dr. Shawn Lockery (U. Oregon). Independent strains for ectopic expression of *S. stercoralis* AFD-rGCs in *C. elegans* ASE (Table S3, strains EAH359, EAH361, EAH365, EAH378, EAH370, EAH372, EAH374, EAH376, and EAH379) were generated by microinjecting test plasmids (pASB57, pASB61, pASB62) into N2 hermaphrodites at 20 ng/μL. Each ectopic expression strain was crossed to XL115 to generate the strains used for calcium imaging (Table S3, strains EAH360, EAH362, EAH366, EAH369, EAH371, EAH373, EAH375, EAH377, and EAH380).

METHOD DETAILS

Phylogenetic Analysis—Identification of rGC genes in *S. stercoralis* and *S. ratti* was based on protein sequence homology with the following *C. elegans* rGCs: ODR-1, DAF-11, GCY-1, GCY-3, GCY-4, GCY-5, GCY-6, GCY-7, GCY-8, GCY-9, GCY-11, GCY-12, GCY-13, GCY-14, GCY-15, GCY-17, GCY-18, GCY-19, GCY-20, GCY-21, GCY-22, GCY-23, GCY-25, GCY-27, GCY-28, and GCY-29. For all *C. elegans* rGCs with multiple isoforms, coding sequences for isoform a were used. Amino acid sequences for *C. elegans* rGCs were retrieved from WormBase (release WS283) and used in TBLASTN searches of *S. stercoralis* and *S. ratti* genomes via WormBase ParaSite (release WBPS16)[66]. For every *C. elegans* rGC, TBLASTN results were sorted by score and overlapping genes for the top 10–30 matches were recorded. Duplicate genes were removed, then parasite genomic sequences and gene annotations were retrieved from WormBase ParaSite and imported into Geneious Prime 2022.0.1. The accuracy of predicted gene models for each parasite gene identified in the TBLASTN search was examined using the following criteria: protein sequence length, identity of InterProScan domain predictions, and overlap of gene model with RNA-seq expression[61,62]. When necessary, gene models were manually adjusted using Geneious Prime. Updated gene models were submitted to WormBase ParaSite and WormBase for dissemination. For a list of all *Strongyloides* and *C. elegans* rGC gene IDs and protein sequences, see Data S1. For a list of manually curated *Strongyloides* rGC genes and descriptions of adjustments made to WBPS16 gene models, see Table S1.

MUSCLE alignment of amino acid sequences was calculated in Geneious Prime. Phylogenetic tree reconstruction was performed on the MUSCLE alignment by applying a maximum-likelihood phylogenetic inference method with IQ-TREE[67] and ModelFinder[68] with ultrafast bootstrapping (1000 replicates), using the WAG substitution matrix[69] with empirical base frequencies and a free-rate substitution model[70,71] with 7 categories. The maximum-likelihood tree was plotted in R v4.1.2 using treedataverse packages (ggtree v3.2.1, tidytree v0.3.6, and treeio v1.18.1)[72,73].

The following *S. stercoralis* and *S. ratti* genes were identified as homologs of the *C. elegans* AFD-specific rGCs based on amino acid sequence homology and phylogenetic clustering: *Ss-gcy-23.1* (SSTP_0000354300), *Ss-gcy-23.2* (SSTP_0000775800), *Ss-gcy-23.3* (SSTP_0000846800), *Sr-gcy-23.1* (SRAE_2000430600), *Sr-gcy-23.2* (SRAE_0000007100), and *Sr-gcy-23.3* (SRAE_X000020900). Percent sequence identity between *C. elegans* AFD-rGCs and *Strongyloides* AFD-rGCs was calculated by performing MUSCLE alignment of the 9 AFD-rGC sequences in Geneious Prime. MUSCLE alignments were run on full-length protein sequences, extracellular domains, intracellular domains, and cyclase domains; domains are InterProScan and PROSITE predictions.

Molecular Biology—Promoter sequences for all *S. stercoralis* genes and *Sr-gcy-23.2* were extracted by PCR-amplifying ~1.7–2 kb upstream of the predicted first exons; some sequences include portions of the first exon. Primers used are listed in Table S4. Putative promoter sequences were cloned into either the *Strongyloides* expression vector pPV254 (containing *Ss-act-2p::GFP*; a gift from Dr. James Lok, UPenn) in place of the *Ss-act-2* promoter, or into a *Strongyloides* promoter-less expression vector (pASB10, which features a multiple cloning site and the *Ss-era-1* 3'UTR[64]) along with *wrmScarlet-I*[74] (obtained from Dr. Hillel Schwartz, Caltech). The following constructs were generated: *Ss-gcy-23.1p::GFP* (pASB51), *Ss-gcy-23.2p::GFP* (pASB41), *Ss-gcy-23.3p::GFP* (pASB42), *Sr-gcy-23.2p::GFP* (pJHL09), *and Sr-gcy-23.2p::wrmScarlet-I* (pASB25).

For expression of HisCl1 in *S. stercoralis* AFD, we first calculated a *Strongyloides* codon-optimized *HisCl1* sequence (*strHisCl1*) by hand[41,75]. To generate a *Sr-gcy-23.2p::strHisCl1* construct (pASB30), *strHisCl1* was synthesized by Genewiz (South Plainfield, NJ) and cloned into pASB10 with the *Sr-gcy-23.2* promoter from pJHL09. For expression of the calcium sensor YC3.60[42] in *S. stercoralis* AFD, we calculated a *Strongyloides* codon-optimized *YC3.60* sequence (*strYC3.60*) by hand. To generate a *Sr-gcy-23.2p::strYC3.60* construct (pASB52), *strYC3.60* was synthetized by Genewiz and cloned into pASB30, replacing *strHisCl1*. For imaging the impact of HisCl1-silencing on *Ss*-AFD activity, we generated a *Sr-gcy-23.2p::strHisCl1::P2A::mRFPmars* construct (pASB56). The *P2A::mRFPmars* sequence was taken from pPV505 (a gift from Dr. James Lok, UPenn)[76]. For expression of the cGMP sensory FlincG3[52,53] in *S. stercoralis* AFD, we first calculated a *Strongyloides* codon-optimized *FlincG3* sequence (*strFlincG3*) using the Wild Worm Codon Adapter[77]. To generate a *Sr-gcy-23.2p::strFlincG3* construct (pASB67), *strFlincG3* was synthesized and subcloned into pJHL09 by GenScript (Piscataway, NJ).

For ectopic expression of *S. stercoralis* AFD-rGCs in *C. elegans* ASE neurons, cDNA sequences were identified based on gene predictions in WormBase ParaSite; in some cases predictions were manually adjusted (see phylogenetic analysis methods, above)[61,66]. Sequences were codon-optimized for *C. elegans* and 2 synthetic introns were inserted into the sequence using the *C. elegans* Codon Adapter[78]. To generate a *flp-6p::Ss-gcy-23.1::SL2::mCherry* construct (pASB57), the cDNA sequence was synthesized by Genewiz and used to modify the plasmid AT1_66, obtained from Dr. Piali Sengupta (Brandeis)[35]. To generate *flp-6p::Ss-gcy-23.2::SL2::mCherry* (pASB61) and *flp-6p::Ss-gcy-23.3::SL2::mCherry* (pASB62) constructs (Table S2), cDNA sequences were synthesized and inserted into AT1_66 by GenScript.

Fluorescent Microscopy—For fluorescent microscopy, the F_1 iL3 progeny of microinjected females were recovered and screened for GFP or wrmScarlet-I expression on a Leica M165 FC fluorescence microscope using a previously established nicotine-paralysis method[46]. Transgenic iL3s were transferred to a small watch glass containing BU saline[79] and allowed to recover overnight. Animals were exposed to 50–100 mM levamisole in BU saline, then mounted on a slide with 5% Noble agar dissolved in BU saline, coverslipped, and sealed with quick-drying nail polish. Epifluorescence and DIC images were taken with a 40x air objective (EC Plan-Neofluar 40x/0.75 ∞/0.17; Zeiss) on an upright Zeiss AxioImager A2 microscope equipped with a 10 filter set for GFP (BP470/20, FT510, BP540/25; Zeiss), a 63 HE filter set for wrmScarlet-I (BP572/25, FT590, BP629/62; Zeiss), a 46 HE filter set for YFP(BP500/25, FT515, BP535/30; Zeiss) and a 47 HE filter set for CFP (BP436/25, FT455, BP480/40; Zeiss), a Hamamatsu W-View Gemini image splitter in bypass mode, and a Hamamatsu ORCA-Flash4.0 camera; broad spectrum fluorescence illumination was provided by an X-Cite Series 210Q lamp. Additional epifluorescence images were taken with a 40x oil objective (Plan-Apochromat 40x/1.4 ∞/0.17 Oil DIC (UV) VIS-IR M27; Zeiss) on an inverted Zeiss AxioObserver microscope equipped with a 38 HE filter set for

GFP (BP470/40, FT495, BP 525/50) and a 63 HE filter set for wrmScarlet-I (BP572/25, FT590, BP629/62), and a Hamamatsu ORCA-Flash4.0 camera; fluorescence illumination was provided by Colibri 7 LEDs (LED-Module 475 nm and LED-Module 567nm). Confocal images were acquired using a Zeiss LSM880 confocal microscope (Broad Stem Cell Research Center, Molecular, Cellular, and Developmental Biology Microscopy Core Facility, UCLA). Images were acquired using Zeiss ZEN 2 (blue edition) software. Image montages were generated using FIJI[80].

Behavioral Assays—Thermotaxis assays were performed using a custom thermoelectric behavioral arena[18]. For experiments quantifying the distribution of a population, worms were monitored using one or two 5 mega-pixel CMOS cameras (BTE-BO50-U, Mightex Systems) at a frame rate of at least 1 frame per minute. The population-level movement of worms was analyzed as previously described[18]. For worm tracking experiments, worm movements were imaged at a frame rate of 0.5 frames per second, and individual iL3 trajectories were quantified *post hoc* as previously described[18], using updated custom MATLAB scripts.

For testing wild-type thermotaxis behaviors across different cultivation temperatures, iL3s were collected from 7–14 day old fecal-charcoal plates using a Baermann apparatus[63] or removed directly from the lid of the fecal-charcoal plate and then stored in a watch glass containing BU saline at either 15°C or 23°C for at least two hours. For negative thermotaxis behaviors, iL3s were placed in a 12–22°C gradient (T_{start} = 14°C, 17°C, or 20°C) for 30 minutes. For positive thermotaxis behaviors, iL3s were placed in a ~21–33°C gradient (T_{start} = 23°C) for 20 minutes. The behavioral data for unstimulated wild-type iL3s (Figure S3B) are from Bryant *et al* 2018[18].

For measuring “U-turn” behaviors, 7–14 day old fecal-charcoal plates were incubated for at least two hours at 15°C or 23°C. iL3s were collected using a Baermann apparatus

or removed directly from the lid of the fecal-charcoal plate and stored in a watch glass containing BU saline at their cultivation temperature for at least two hours. Two thermal gradients were used to elicit U-turn behaviors: a 12–22°C gradient (T_{start} = 20°C) and a 15–25°C gradient (T_{start} = 23°C). For testing the percentage of the population that engaged in U-turn behaviors, at least 150 iL3s were placed on a thermotaxis plate and their migration was imaged for 20–30 minutes. For tracking individual iL3 trajectories during U-turns, either single iL3s or a small group (<100) of iL3s were placed on a thermotaxis plate and their migration was imaged for 20 min.

For testing negative thermotaxis by *Ss-tax-4* iL3s, either *Ss-tax-4* iL3s or no-Cas9 control iL3s were screened for mRFPmars expression as previously described[18,46]. 1–2 mRFPmars-expressing *S. stercoralis* iL3s were placed at 20°C in a ~17–26°C gradient for 15 min. Following the cessation of recording, single iL3s were recollected for individual genomic DNA preparations. mRFPmars-positive iL3s in which *Ss-tax-4* expression was fully disrupted either by deletion or integration events (*i.e., Ss-tax-4* iL3s) were identified by *post-hoc* single-worm genotyping, as previously described[18,46]. Trajectories of *Ss-tax-4* iL3s were tracked and quantified following *post-hoc* genotyping.

For testing the effect of HisCl1-mediated AFD silencing on positive and negative thermotaxis, *Sr-gcy-23.2p::strHisCl1* + *Sr-gcy-23.2p::GFP* iL3s were screened for GFP expression as follows: F_1 iL3 progeny of microinjected females were recovered from fecal-charcoal cultures using a Baermann apparatus and stored in a small watch glass containing 2–3 mL BU saline. ~10 μL of iL3-containing BU saline was placed on a 2% NGM plate containing a lawn of OP50 and migrating iL3s were screened at low magnification for strong GFP expression. Recovered iL3s were evenly split into two watch glasses containing either BU saline or BU saline + 20–50 mM histamine. Watch glasses were incubated at 23°C for at least 2 h. For behavioral experiments, iL3s were transferred in batches (<20 worms per experiment) to 3% thermotaxis agar plates[18,81] with or without 10 mM histamine. For positive thermotaxis assays, iL3s were placed at 30°C in a ~22–34°C gradient; for negative thermotaxis assays, iL3s were placed at 20°C in a ~17–26°C gradient. For both positive and negative thermotaxis, assay duration was 10 min. On individual experimental days, behavioral assays were always conducted with paired histamine-positive and no-histamine control experiments. Furthermore, the researcher performing the assay was fully blinded to the experimental condition: blinding was implemented as recovered GFP-positive iL3s were split into BU saline or BU saline + histamine watch glasses (*i.e.,* the researcher splitting the population was unaware of which watch glass contained histamine-spiked BU saline). Blinding was lifted only following *post-hoc* tracking.

Calcium and cGMP Imaging—For imaging of *Ss*-AFD activity, the F_1 iL3 progeny of microinjected females were recovered and screened for the presence of either YC3.60 or FlincG3 using methods previously established for fluorescent screening of nicotine-paralyzed transgenic iL3s[46]. Prior to imaging, *C. elegans* adults on 2% NGM plates with an OP50 lawn or *S. stercoralis* iL3s in BU saline-containing watch glasses were incubated overnight at either 23°C or 15°C. Animals were exposed to 100 mM levamisole in BU saline (*S. stercoralis* iL3s) or 10 mM levamisole in M9 saline (*C. elegans* adults), then mounted

on a slide with 5% Noble agar dissolved in BU or M9 saline, coverslipped, and sealed with quick-drying nail polish.

YC3.60 imaging was performed with a 40x air objective (EC Plan-Neofluar 40x/0.75 ∞/0.17; Zeiss) on an upright Zeiss AxioImager A2 microscope equipped with a 78 HE ms filter set (BP445/25 + BP510/15, DFT460+520 + FT510, BP480/22 + LP530; Zeiss), a Hamamatsu W-View Gemini image splitter with a CFP/YFP dual camera filter set, and a Hamamatsu ORCA-Flash4.0 camera for simultaneous acquisition of CFP and YFP images. FlincG3 imaging was performed with a 40x air objective (EC Plan-Neofluar 40x/0.75 ∞/0.17; Zeiss) on an upright Zeiss AxioImager A2 microscope with a 10 filter set (BP470/20, FT510, BP540/25; Zeiss), a Hamamatsu W-View Gemini image splitter in bypass mode, and a Hamamatsu ORCA-Flash4.0 camera. Broad spectrum fluorescence illumination was provided by a X-Cite Series 210Q lamp. For both YC3.60 and FlincG3, images were acquired every 250 ms using the Zeiss ZEN software with a time lapse module.

Temperature ramps were delivered to slide-mounted worms using a custom thermal stimulator (Figure S4A) based on established *C. elegans* systems[45]. An annular-style Peltier element (430533-502, Laird Thermal Systems) was mounted on a custom aluminum heat block held on the microscope stage with a custom 3D-printed stage clamp. The custom heat block was attached to a temperature-controlled recirculating water bath (13–874-180, Fisher Scientific) set to the ambient cultivation temperature. The Peltier element was controlled by a closed-loop control circuit consisting of a PID controller (ATEC302, Accuthermo Technology), an H-bridge amplifier (FTX700D, Accuthermo Technology), two 12 V, 30 W AC/DC power converters (LS35–12, TDK-Lambda Americas Inc), and a 10 kΩ thermistor (USP12837, Littelfuse) that was attached to the coverslip near the immobilized worm with adhesive tape. Slides containing worms were placed on the Peltier element; halocarbon oil was placed between the Peltier element and the glass slide to ensure strong thermal transfer. Slides were anchored to the aluminum heat block using adhesive tape. Prior to the start of imaging, slides were brought to cultivation temperature (23°C or 15°C) for 5 min using the ATEC302 software general control mode. Thus, for all experiments, the recently experienced holding temperature (T_H) was equivalent to T_C; we refer to this combined ambient temperature as $T_{ambient}$. During imaging, temperature ramps were delivered using the ATEC302 software programmable step temperature control function. A full list of all thermal ramps used in this study is provided in Table S5. Measured temperatures at the coverslip surface were recorded using the ATEC302 software data log function.

From time-lapse dual-wavelength images containing aligned CFP and YFP signals (YC3.60 imaging) or from time-lapse images containing GFP signals (FlincG3 imaging), we calculated the mean intensity over time for soma and background regions of interest (ROI) using the ZEN software. CSV files containing imaging data and temperature log files were saved, then processed using custom MATLAB scripts. For YC3.60 imaging, CFP and YFP signals from soma and background ROIs were used to calculate the baseline-corrected YFP/CFP ratio (% $\Delta R/R_0$); YFP signals were corrected for bleed-through from the CFP channel. For FlincG3 imaging, GFP signals from lamellar sensory tips and background ROIs were used to calculate the baseline-corrected GFP signal (% $\Delta F/F_0$). For both YC3.60 and FlincG3, responses were aligned relative to the ATEC302 temperature log based on file

time stamps. Plots of aligned fluorescence responses and temperature records were saved as EPS files. For heatmaps, individual fluorescence traces (heatmap rows) were ordered using average linkage clustering; heatmap colors were defined using the viridis color map.

Custom MATLAB code was used to calculate: linear/monotonic regressions at different temperature windows, thermal threshold (either T^*_{AFD} or T^*_{ASE}), temperatures eliciting maximal and minimal fluorescence responses, and the response magnitude at the steady-state stimulus temperature (either the warmest or coldest temperature in the stimulus), across different time windows. For AFD recordings, thermal threshold (T^*_{AFD}) is defined as the first temperature where the absolute value of the AFD response is at least 3*STD from the response at T_0 for the amount of time it takes the warming/cooling temperature ramp to change 0.25°C (10 s). For *C. elegans* ectopic expression recordings, to control for the possibility of native *Ce*-ASE temperature responses at warm temperatures, the thermal threshold (T^*_{ASE}) was defined as the first temperature where the absolute value of the *Ce*-$ASE_{experimental}$ response deviates from the average *Ce*-ASE_{WT} response by at least 3*STD for a minimum of 40 seconds.

For imaging the effect of HisCl1 on *Ss*-AFD neurons, *Sr-gcy-23.2p::strHisCl1::P2A::mRFPmars* + *Sr-gcy-23.2p::strYC3.60* iL3s were screened for co-expression of HisCl1 and YC3.60 via the nicotine-paralysis method described above. Transgenic iL3s were incubated in BU overnight at 23°C, then transferred to a watch glass containing either BU (control animals) or BU + 50 mM histamine (experimental animals) for at least 2 hours, at 23°C. For imaging, experimental animals were exposed to 100 mM levamisole + 50 mM histamine in BU saline, then mounted on a slide with 5% Noble agar dissolved in 50 mM histamine in BU, coverslipped, and sealed with quick-drying nail polish. For control animals, mounting solutions and agar did not contain histamine. To quantify the impact of HisCl1-silencing on *Ss*-AFD temperature responses, we calculated the sum of the absolute deviation from baseline during the warming phase of the temperature stimulus (21–33°C). Baseline was defined as the AFD response at T_0 (20°C).

QUANTIFICATION AND STATISTICAL ANALYSIS

Statistical analyses were conducted using GraphPad Prism 9. Exact *p* values for all statistical tests are provided in Data S2. Statistical details of experiments are provided in figure legends and Data S2. Power analyses to determine appropriate sample sizes were conducted using G*Power 3.1[82]. For plotting single-worm tracking quantifications and neural imaging quantifications, data were imported into R v4.1.2 and plotted using the ggplot2 package v3.3.5[83].

Supplementary Material

Refer to Web version on PubMed Central for supplementary material.

Acknowledgements

We gratefully acknowledge Dirk Williams and the UCLA R&D Shops, as well as the UCLA MCDB/BSCRC microscopy core. We thank Dr. Josh Hawk for advice related to the design of thermal stimulators for calcium imaging. We also thank Dr. Piali Sengupta for advice related to the naming of *Strongyloides* AFD-rGCs. We

thank Dr. Johnathan Stoltzfus and Damia Gonzalez Akimori for advice related to manual curation of parasite gene annotations. We thank WormBase and WormBase ParaSite. We thank Dr. Pavak Shah, Dr. Michelle Castelletto, Dr. Ruhi Patel, and Dr. Kelly Zalocusky for insightful comments on the manuscript. This work was funded by an A.P. Giannini Postdoctoral Fellowship (A.S.B.); and a Burroughs-Wellcome Fund Investigators in the Pathogenesis of Disease Award, Howard Hughes Medical Institute Faculty Scholar Award, and National Institutes of Health R01AI136976 (E.A.H.).

References

1. Beknazarova M, Whiley H, and Ross K (2016). Strongyloidiasis: a disease of socioeconomic disadvantage. Int J Environ Res Public Health 13, 517.
2. Bethony J, Brooker S, Albonico M, Geiger SM, Loukas A, Diemert D, and Hotez PJ (2006). Soil-transmitted helminth infections: ascariasis, trichuriasis, and hookworm. Lancet 367, 1521–1532. [PubMed: 16679166]
3. Lustigman S, Prichard RK, Gazzinelli A, Grant WN, Boatin BA, McCarthy JS, and Basáñez M-G (2012). A research agenda for helminth diseases of humans: the problem of helminthiases. PLoS Negl Trop Dis 6, e1582. [PubMed: 22545164]
4. McKenna ML, McAtee S, Bryan PE, Jeun R, Ward T, Kraus J, Bottazzi ME, Hotez PJ, Flowers CC, and Mejia R (2017). Human intestinal parasite burden and poor sanitation in rural Alabama. Am J Trop Med Hyg 97, 1623–1628. [PubMed: 29016326]
5. Singer R, Xu TH, Herrera LNS, Villar MJ, Faust KM, Hotez PJ, Aiken ARA, and Mejia R (2020). Prevalence of intestinal parasites in a low-income Texas community. Am J Trop Med Hyg 102, 1386–1395. [PubMed: 32207401]
6. Nutman TB (2017). Human infection with *Strongyloides stercoralis* and other related *Strongyloides* species. Parasitology 144, 263–273. [PubMed: 27181117]
7. Schafer TW, and Skopic A (2006). Parasites of the small intestine. Curr Gastroenterol Rep 8, 312–320. [PubMed: 16836943]
8. Buonfrate D, Requena-Mendez A, Angheben A, Muñoz J, Gobbi F, Van Den Ende J, and Bisoffi Z (2013). Severe strongyloidiasis: a systematic review of case reports. BMC Infect Dis 13, 78. [PubMed: 23394259]
9. Diawara A, Schwenkenbecher JM, Kaplan RM, and Prichard RK (2013). Molecular and biological diagnostic tests for monitoring benzimidazole resistance in human soil-transmitted helminths. Am J Trop Med Hyg 88, 1052–1061. [PubMed: 23458960]
10. Keiser J, and Utzinger J (2008). Efficacy of current drugs against soil-transmitted helminth infections: systematic review and meta-analysis. JAMA 299, 1937–1948. [PubMed: 18430913]
11. Learmount J, Stephens N, Boughtflower V, Barrecheguren A, and Rickell K (2016). The development of anthelmintic resistance with best practice control of nematodes on commercial sheep farms in the UK. Vet Parasitol 229, 9–14. [PubMed: 27809985]
12. Repetto SA, Ruybal P, Batalla E, López C, Fridman V, Sierra M, Radisic M, Bravo PM, Risso MG, González Cappa SM, et al. (2018). Strongyloidiasis outside endemic areas: long-term parasitological and clinical follow-up after ivermectin treatment. Clin Infect Dis 66, 1558–1565. [PubMed: 29360939]
13. Buonfrate D, Bisanzio D, Giorli G, Odermatt P, Fürst T, Greenaway C, French M, Reithinger R, Gobbi F, Montresor A, et al. (2020). The global prevalence of *Strongyloides stercoralis* infection. Pathogens 9, 468.
14. Tamarozzi F, Martello E, Giorli G, Fittipaldo A, Staffolani S, Montresor A, Bisoffi Z, and Buonfrate D (2019). Morbidity associated with chronic *Strongyloides stercoralis* infection: a systematic review and meta-analysis. Am J Trop Med Hyg 100, 1305–1311. [PubMed: 30963990]
15. De Wilton A, Nabarro LE, Godbole GS, Chiodini PL, Boyd A, and Woods K (2021). Risk of *Strongyloides* Hyperinfection Syndrome when prescribing dexamethasone in severe COVID-19. Travel Med Infect Dis 40, 101981. [PubMed: 33535106]
16. Stauffer WM, Alpern JD, and Walker PF (2020). Covid-19 and dexamethasone: a potential strategy to avoid steroid-related *Strongyloides* hyperinfection. JAMA 324, 623–624. [PubMed: 32761166]

17. Bryant AS, and Hallem EA (2018). Terror in the dirt: Sensory determinants of host seeking in soil-transmitted mammalian-parasitic nematodes. Int J Parasitol Drugs Drug Resist 8, 496–510. [PubMed: 30396862]
18. Bryant AS, Ruiz F, Gang SS, Castelletto ML, Lopez JB, and Hallem EA (2018). A critical role for thermosensation in host seeking by skin-penetrating nematodes. Curr Biol 28, 2338–2347. [PubMed: 30017486]
19. Gang SS, Castelletto ML, Yang E, Ruiz F, Brown TM, Bryant AS, Grant WN, and Hallem EA (2020). Chemosensory mechanisms of host seeking and infectivity in skin-penetrating nematodes. Proc Natl Acad Sci USA 117, 17913–17923. [PubMed: 32651273]
20. Bryant AS, and Hallem EA (2018). Temperature-dependent behaviors of parasitic helminths. Neurosci Lett 687, 290–303. [PubMed: 30336196]
21. Hedgecock EM, and Russell RL (1975). Normal and mutant thermotaxis in the nematode *Caenorhabditis elegans*. Proc Natl Acad Sci USA 72, 4061–4065. [PubMed: 1060088]
22. Wittenburg N, and Baumeister R (1999). Thermal avoidance in *Caenorhabditis elegans*: an approach to the study of nociception. Proc Natl Acad Sci USA 96, 10477–10482. [PubMed: 10468634]
23. Glauser DA, Chen WC, Agin R, Macinnis BL, Hellman AB, Garrity PA, Tan MW, and Goodman MB (2011). Heat avoidance is regulated by transient receptor potential (TRP) channels and a neuropeptide signaling pathway in *Caenorhabditis elegans*. Genetics 188, 91–103. [PubMed: 21368276]
24. Garrity PA, Goodman MB, Samuel AD, and Sengupta P (2010). Running hot and cold: behavioral strategies, neural circuits, and the molecular machinery for thermotaxis in *C. elegans* and *Drosophila*. Genes Dev. 24, 2365–2382. [PubMed: 21041406]
25. Schild LC, and Glauser DA (2013). Dynamic switching between escape and avoidance regimes reduces *Caenorhabditis elegans* exposure to noxious heat. Nat Commun 4, 2198. [PubMed: 23887613]
26. Goodman MB, and Sengupta P (2018). The extraordinary AFD thermosensor of *C. elegans*. Pflugers Arch 470, 839–849. [PubMed: 29218454]
27. Takeishi A, Takagaki N, and Kuhara A (2020). Temperature signaling underlying thermotaxis and cold tolerance in *Caenorhabditis elegans*. J Neurogenet 34, 351–362. [PubMed: 32316810]
28. Mori I, and Ohshima Y (1995). Neural regulation of thermotaxis in *Caenorhabditis elegans*. Nature 376, 344–348. [PubMed: 7630402]
29. Chung SH, Clark DA, Gabel CV, Mazur E, and Samuel ADT (2006). The role of the AFD neuron in *C. elegans* thermotaxis analyzed using femtosecond laser ablation. BMC Neurosci 7, 30. [PubMed: 16600041]
30. Luo L, Cook N, Venkatachalam V, Martinez-Velazquez LA, Zhang X, Calvo AC, Hawk J, MacInnis BL, Frank M, Ng JHR, et al. (2014). Bidirectional thermotaxis in *Caenorhabditis elegans* is mediated by distinct sensorimotor strategies driven by the AFD thermosensory neurons. Proc Natl Acad Sci USA 111, 2776–2781. [PubMed: 24550307]
31. Wasserman SM, Beverly M, Bell HW, and Sengupta P (2011). Regulation of response properties and operating range of the AFD thermosensory neurons by cGMP signaling. Curr Biol 21, 353–362. [PubMed: 21315599]
32. Ashton FT, Bhopale VM, Fine AE, and Schad GA (1995). Sensory neuroanatomy of a skin-penetrating nematode parasite: *Strongyloides stercoralis*. I. Amphidial neurons. J Comp Neurol 357, 281–295. [PubMed: 7665730]
33. Lopez PM, Boston R, Ashton FT, and Schad GA (2000). The neurons of class ALD mediate thermotaxis in the parasitic nematode, *Strongyloides stercoralis*. Int J Parasitol 30, 1115–1121. [PubMed: 10996330]
34. Ashton FT, Li J, and Schad GA (1999). Chemo- and thermosensory neurons: structure and function in animal parasitic nematodes. Vet Parasitol 84, 297–316. [PubMed: 10456420]
35. Takeishi A, Yu YV, Hapiak VM, Bell HW, O'Leary T, and Sengupta P (2016). Receptor-type guanylyl cyclases confer thermosensory responses in *C. elegans*. Neuron 90, 235–244. [PubMed: 27041501]

36. Ramot D, MacInnis BL, and Goodman MB (2008). Bidirectional temperature-sensing by a single thermosensory neuron in *C. elegans*. Nat Neurosci 11, 908–915. [PubMed: 18660808]
37. Inada H, Ito H, Satterlee J, Sengupta P, Matsumoto K, and Mori I (2006). Identification of guanylyl cyclases that function in thermosensory neurons of *Caenorhabditis elegans*. Genetics 172, 2239–2252. [PubMed: 16415369]
38. Wang D, O'Halloran D, and Goodman MB (2013). GCY-8, PDE-2, and NCS-1 are critical elements of the cGMP-dependent thermotransduction cascade in the AFD neurons responsible for *C. elegans* thermotaxis. J Gen Physiol 142, 437–449. [PubMed: 24081984]
39. Fitzpatrick DA, O'Halloran DM, and Burnell AM (2006). Multiple lineage specific expansions within the guanylyl cyclase gene family. BMC Evol Biol 6, 26. [PubMed: 16549024]
40. Ortiz CO, Etchberger JF, Posy SL, Frøkjær-Jensen C, Lockery S, Honig B, and Hobert O (2006). Searching for neuronal left/right asymmetry: genomewide analysis of nematode receptor-type guanylyl cyclases. Genetics 173, 131–149. [PubMed: 16547101]
41. Pokala N, Liu Q, Gordus A, and Bargmann CI (2014). Inducible and titratable silencing of *Caenorhabditis elegans* neurons *in vivo* with histamine-gated chloride channels. Proc Natl Acad Sci USA 111, 2770–2775. [PubMed: 24550306]
42. Nagai T, Yamada S, Tominaga T, Ichikawa M, and Miyawaki A (2004). Expanded dynamic range of fluorescent indicators for Ca2+ by circularly permuted yellow fluorescent proteins. Proc Natl Acad Sci USA 101, 10554–10559. [PubMed: 15247428]
43. Clark DA, Biron D, Sengupta P, and Samuel ADT (2006). The AFD sensory neurons encode multiple functions underlying thermotactic behavior in *Caenorhabditis elegans*. J Neurosci 26, 7444–7451. [PubMed: 16837592]
44. Kimura KD, Miyawaki A, Matsumoto K, and Mori I (2004). The *C. elegans* thermosensory neuron AFD responds to warming. Curr Biol 14, 1291–1295. [PubMed: 15268861]
45. Hawk JD, Calvo AC, Liu P, Almoril-Porras A, Aljobeh A, Torruella-Suárez ML, Ren I, Cook N, Greenwood J, Luo L, et al. (2018). Integration of plasticity mechanisms within a single sensory neuron of *C. elegans* actuates a memory. Neuron 97, 356–367. [PubMed: 29307713]
46. Gang SS, Castelletto ML, Bryant AS, Yang E, Mancuso N, Lopez JB, Pellegrini M, and Hallem EA (2017). Targeted mutagenesis in a human-parasitic nematode. PLoS Pathog 13, e1006675. [PubMed: 29016680]
47. Komatsu H, Mori I, Rhee JS, Akaike N, and Ohshima Y (1996). Mutations in a cyclic nucleotide-gated channel lead to abnormal thermosensation and chemosensation in *C. elegans*. Neuron 17, 707–718. [PubMed: 8893027]
48. Coburn CM, and Bargmann CI (1996). A putative cyclic nucleotide-gated channel is required for sensory development and function in *C. elegans*. Neuron 17, 695–706. [PubMed: 8893026]
49. Gray JM, Hill JJ, and Bargmann CI (2005). A circuit for navigation in *Caenorhabditis elegans*. Proceedings of the National Academy of Sciences 102, 3184–3191.
50. Nguyen PAT, Liou W, Hall DH, and Leroux MR (2014). Ciliopathy proteins establish a bipartite signaling compartment in a *C. elegans* thermosensory neuron. Journal of Cell Science 127, 5317–5330. [PubMed: 25335890]
51. Gong J, Liu J, Ronan EA, He F, Cai W, Fatima M, Zhang W, Lee H, Li Z, Kim G-H, et al. (2019). A cold-sensing receptor encoded by a glutamate receptor gene. Cell 178, 1375–1386.e11. [PubMed: 31474366]
52. Bhargava Y, Hampden-Smith K, Chachlaki K, Wood KC, Vernon J, Allerston CK, Batchelor AM, and Garthwaite J (2013). Improved genetically-encoded, FlincG-type fluorescent biosensors for neural cGMP imaging. Front. Mol. Neurosci 6.
53. Woldemariam S, Nagpal J, Hill T, Li J, Schneider MW, Shankar R, Futey M, Varshney A, Ali N, Mitchell J, et al. (2019). Using a robust and sensitive GFP-based cGMP sensor for real time imaging in intact *Caenorhabditis elegans*. Genetics, genetics.302392.2019.
54. Han Z, Boas S, and Schroeder NE (2016). Unexpected variation in neuroanatomy among diverse nematode species. Front. Neuroanat. 9, 162. [PubMed: 26778973]
55. Hong RL, Riebesell M, Bumbarger DJ, Cook SJ, Carstensen HR, Sarpolaki T, Cochella L, Castrejon J, Moreno E, Sieriebriennikov B, et al. (2019). Evolution of neuronal anatomy and circuitry in two highly divergent nematode species. eLife 8, e47155. [PubMed: 31526477]

56. Schafer W (2016). Nematode nervous systems. Current Biology 26, R955–R959. [PubMed: 27780068]
57. Schulenburg H, and Félix M-A (2017). The natural biotic environment of *Caenorhabditis elegans*. Genetics 206, 55–86. [PubMed: 28476862]
58. Roberts LS, and Janovy J (2005). Gerald D. Schmidt & Larry S. Roberts' Foundations of Parasitology 7th ed. (McGraw-Hill).
59. Yu YV, Bell HW, Glauser DA, VanHooser SD, Goodman MB, and Sengupta P (2014). CaMKI-Dependent regulation of sensory gene expression mediates experience-dependent plasticity in the operating range of a thermosensory neuron. Neuron 84, 919–926. [PubMed: 25467978]
60. Biron D, Shibuya M, Gabel C, Wasserman SM, Clark DA, Brown A, Sengupta P, and Samuel ADT (2006). A diacylglycerol kinase modulates long-term thermotactic behavioral plasticity in *C. elegans*. Nat Neurosci 9, 1499–1505. [PubMed: 17086178]
61. Hunt VL, Tsai IJ, Coghlan A, Reid AJ, Holroyd N, Foth BJ, Tracey A, Cotton JA, Stanley EJ, Beasley H, et al. (2016). The genomic basis of parasitism in the *Strongyloides* clade of nematodes. Nat Genet 48, 299–307. [PubMed: 26829753]
62. Stoltzfus JD, Minot S, Berriman M, Nolan TJ, and Lok JB (2012). RNAseq analysis of the parasitic nematode *Strongyloides stercoralis* reveals divergent regulation of canonical dauer pathways. PLoS Negl Trop Dis 6, e1854. [PubMed: 23145190]
63. Lok JB (2007). *Strongyloides stercoralis*: a model for translational research on parasitic nematode biology. WormBook, 1–18.
64. Junio AB, Li X, Massey HC, Nolan TJ, Todd Lamitina S, Sundaram MV, and Lok JB (2008). *Strongyloides stercoralis*: cell- and tissue-specific transgene expression and co-transformation with vector constructs incorporating a common multifunctional 3' UTR. Exp Parasitol 118, 253–265. [PubMed: 17945217]
65. Stiernagle T (2006). Maintenance of *C. elegans*. WormBook, 1–11, http://www.wormbook.org.
66. Howe KL, Bolt BJ, Shafie M, Kersey P, and Berriman M (2017). WormBase ParaSite − a comprehensive resource for helminth genomics. Mol Biochem Parasitol 215, 2–10. [PubMed: 27899279]
67. Nguyen L-T, Schmidt HA, von Haeseler A, and Minh BQ (2015). IQ-TREE: a fast and effective stochastic algorithm for estimating maximum-likelihood phylogenies. Mol Biol Evol 32, 268–274. [PubMed: 25371430]
68. Kalyaanamoorthy S, Minh BQ, Wong TKF, von Haeseler A, and Jermiin LS (2017). ModelFinder: fast model selection for accurate phylogenetic estimates. Nat Methods 14, 587–589. [PubMed: 28481363]
69. Whelan S, and Goldman N (2001). A general empirical model of protein evolution derived from multiple protein families using a maximum-likelihood approach. Molecular Biology and Evolution 18, 691–699. [PubMed: 11319253]
70. Soubrier J, Steel M, Lee MSY, Der Sarkissian C, Guindon S, Ho SYW, and Cooper A (2012). The influence of rate heterogeneity among sites on the time dependence of molecular rates. Molecular Biology and Evolution 29, 3345–3358. [PubMed: 22617951]
71. Yang Z (1995). A space-time process model for the evolution of DNA sequences. Genetics 139, 993–1005. [PubMed: 7713447]
72. Wang L-G, Lam TT-Y, Xu S, Dai Z, Zhou L, Feng T, Guo P, Dunn CW, Jones BR, Bradley T, et al. (2020). Treeio: an R package for phylogenetic tree input and output with richly annotated and associated data. Molecular Biology and Evolution 37, 599–603. [PubMed: 31633786]
73. Yu G (2020). Using ggtree to visualize data on tree-like structures. Current Protocols in Bioinformatics 69.
74. El Mouridi S, Lecroisey C, Tardy P, Mercier M, Leclercq-Blondel A, Zariohi N, and Boulin T (2017). Reliable CRISPR/Cas9 genome engineering in *Caenorhabditis elegans* using a single efficient sgRNA and an easily recognizable phenotype. G3 7, 1429–1437. [PubMed: 28280211]
75. Mitreva M, Wendl MC, Martin J, Wylie T, Yin Y, Larson A, Parkinson J, Waterston RH, and McCarter JP (2006). Codon usage patterns in Nematoda: analysis based on over 25 million codons in thirty-two species. Genome Biol 7, R75. [PubMed: 26271136]

76. Lok JB, Shao H, Massey HC, and Li X (2017). Transgenesis in *Strongyloides* and related parasitic nematodes: historical perspectives, current functional genomic applications and progress towards gene disruption and editing. Parasitology 144, 327–342. [PubMed: 27000743]

77. Bryant AS, and Hallem EA (2021). The Wild Worm Codon Adapter: a web tool for automated codon adaptation of transgenes for expression in non- *Caenorhabditis* nematodes. G3 (Bethesda) 11, jkab146.

78. Redemann S, Schloissnig S, Ernst S, Pozniakowsky A, Ayloo S, Hyman AA, and Bringmann H (2011). Codon adaptation-based control of protein expression in *C. elegans*. Nat Methods 8, 250–252. [PubMed: 21278743]

79. Hawdon JM, and Schad GA (1991). Long-term storage of hookworm infective larvae in buffered saline solution maintains larval responsiveness to host signals. J Helm Soc Wash 58, 140–142.

80. Schindelin J, Arganda-Carreras I, Frise E, Kaynig V, Longair M, Pietzsch T, Preibisch S, Rueden C, Saalfeld S, Schmid B, et al. (2012). Fiji: an open-source platform for biological-image analysis. Nat. Methods 9, 676–682. [PubMed: 22743772]

81. Goodman MB (2014). Thermotaxis navigation behavior. WormBook, 1–10.

82. Faul F, Erdfelder E, Buchner A, and Lang A-G (2009). Statistical power analyses using G*Power 3.1: tests for correlation and regression analyses. Behav Res Methods 41, 1149–1160. [PubMed: 19897823]

83. Wickham H (2009). Ggplot2: elegant graphics for data analysis (Springer).

Highlights

- *S. stercoralis* senses temperature via the conserved AFD sensory neuron pair
- Heat seeking by *S. stercoralis* infective larvae requires *Ss*-AFD neurons
- *Ss*-AFD neurons display unique temperature-encoding strategies
- Three receptor-type guanylate cyclases in *Ss*-AFD sense body heat

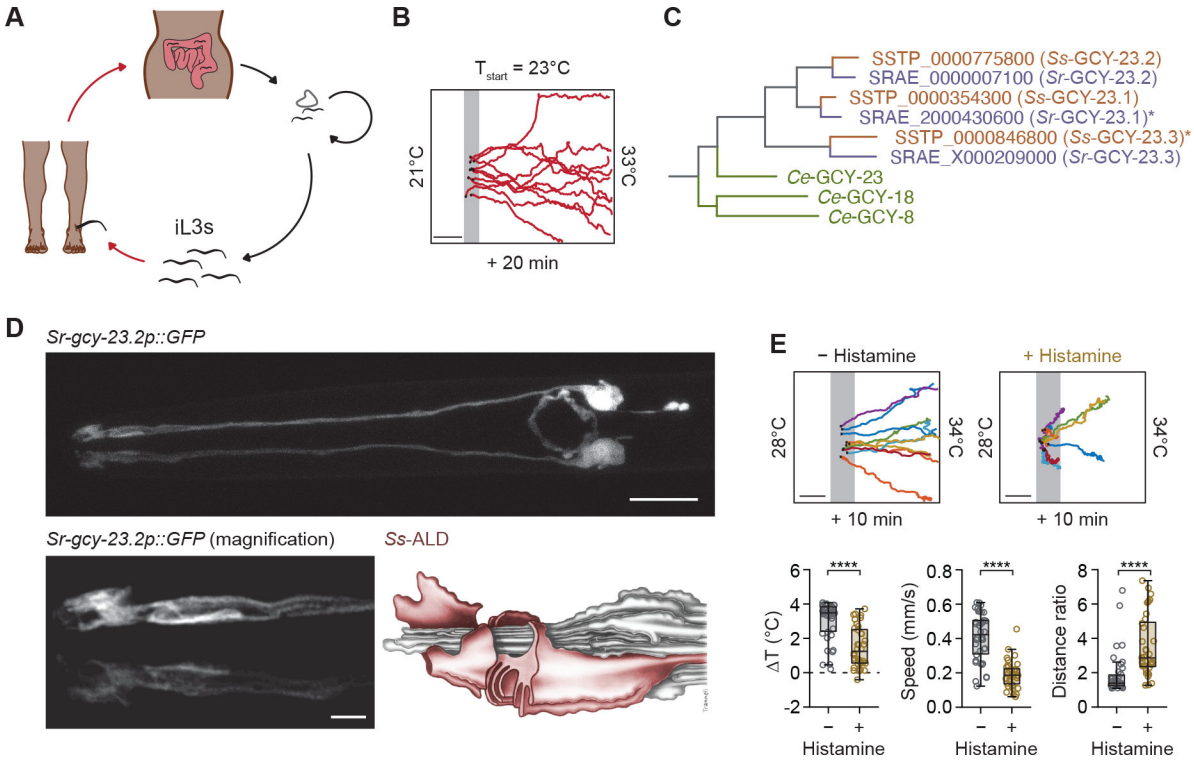

Figure 1. The *S. stercoralis* AFD neurons are required for positive thermotaxis toward host body temperatures.

A. Overview of the life cycle of *S. stercoralis.* Soil-dwelling infective larvae (iL3s) actively seek out hosts using host-emitted sensory cues and infect via skin penetration. Parasitic adults reside in the host small intestine. Their progeny exit the host in feces, and can cycle through a single free-living generation on feces before developmentally arresting as iL3s. For *S. stercoralis* and other mammalian-parasitic worms, host detection and subsequent infection require thermal cues. **B.** Tracks of *S. stercoralis* iL3s engaging in positive thermotaxis toward host body temperatures. Worms were placed at 23°C in a ~21–33°C gradient and allowed to migrate for 20 min. **C.** Phylogenetic tree of *C. elegans* AFD-specific receptor-type guanylate cyclases (AFD-rGCs, green text) and homologous *S. stercoralis* (orange text) and *S. ratti* (purple text) proteins. Tree is a subset from a phylogenetic comparison of all known rGCs in *C. elegans*, *S. stercoralis*, and *S. ratti* (Figure S1). AFD-rGCs for *Strongyloides* spp. were identified based on protein sequence homology with *C. elegans* GCY-8, GCY-18, and GCY-23. SSTP and SRAE numbers indicate *S. stercoralis* and *S. ratti* WormBase ParaSite (WBPS) gene IDs, respectively; gene names indicating homology to *C. elegans* GCY-23 (GCY-23.1, GCY-23.2, and GCY-23.3) for *S. stercoralis* and *S. ratti* sequences are shown in parentheses. For genes marked with an asterisk, predicted gene annotations from WBPS were manually adjusted based on protein sequence, InterProScan domain predictions, and RNA-seq evidence[61,62]. See also Figure S1, Table S1, Data S1. **D.** The promoter region for *Sr-gcy-23.2* drives GFP expression in a single neuron pair (top) with a dendritic morphology (bottom left) that matches the lamellar morphology of *S. stercoralis* ALD (bottom right; EM reconstruction modified from Ashton *et al.*, 1995 and Lopez *et al.*, 2000 with permission; figure reproduced from

Bryant and Hallem, 2018b with permission)[20,32,33]. For top image, scale bar is 10 μm. For bottom left image, scale bar is 2 μm. For all images, anterior is to the left. See also Figure S2. **E.** HisCl1-mediated silencing of the *S. stercoralis* AFD neuron pair results in profound reductions in positive thermotaxis by iL3s. *Top:* Tracks of *Sr-gcy-23.2p::strHisCl1*; *Sr-gcy-23.2p::GFP* iL3s treated with BU saline or histamine (20–50 mM) in BU for at least 1 h, migrating in a ~22–34°C gradient for 10 min. T_{start} = 30°C. *Bottom*: Change in temperature, average speed, and curvature of worm tracks (distance ratio = total distance ÷ maximum displacement; a greater distance ratio indicates a more curved worm trajectory) exhibited by individual iL3s. Exposure to temperatures above ambient and below host body heat increases the speed of wild-type iL3s and reduces track curvature[18]; these effects are reduced when *Ss*-AFD activity is suppressed. n = 38 worms (6 assays, across 6 days) for iL3s treated with BU saline, 36 worms (7 assays, across 7 days) for histamine-treated iL3s; ****p<0.0001, two-sided Mann-Whitney test. Exact p values for all figures are provided in Data S2. For all plots of worm tracks: Scale bar = 2 cm, gray zone = 1°C centered at T_{start}. Black dots show the starting position of the worms. A subset of 10 randomly selected tracks is plotted and only a portion of the full gradient is shown. See also Figure S3.

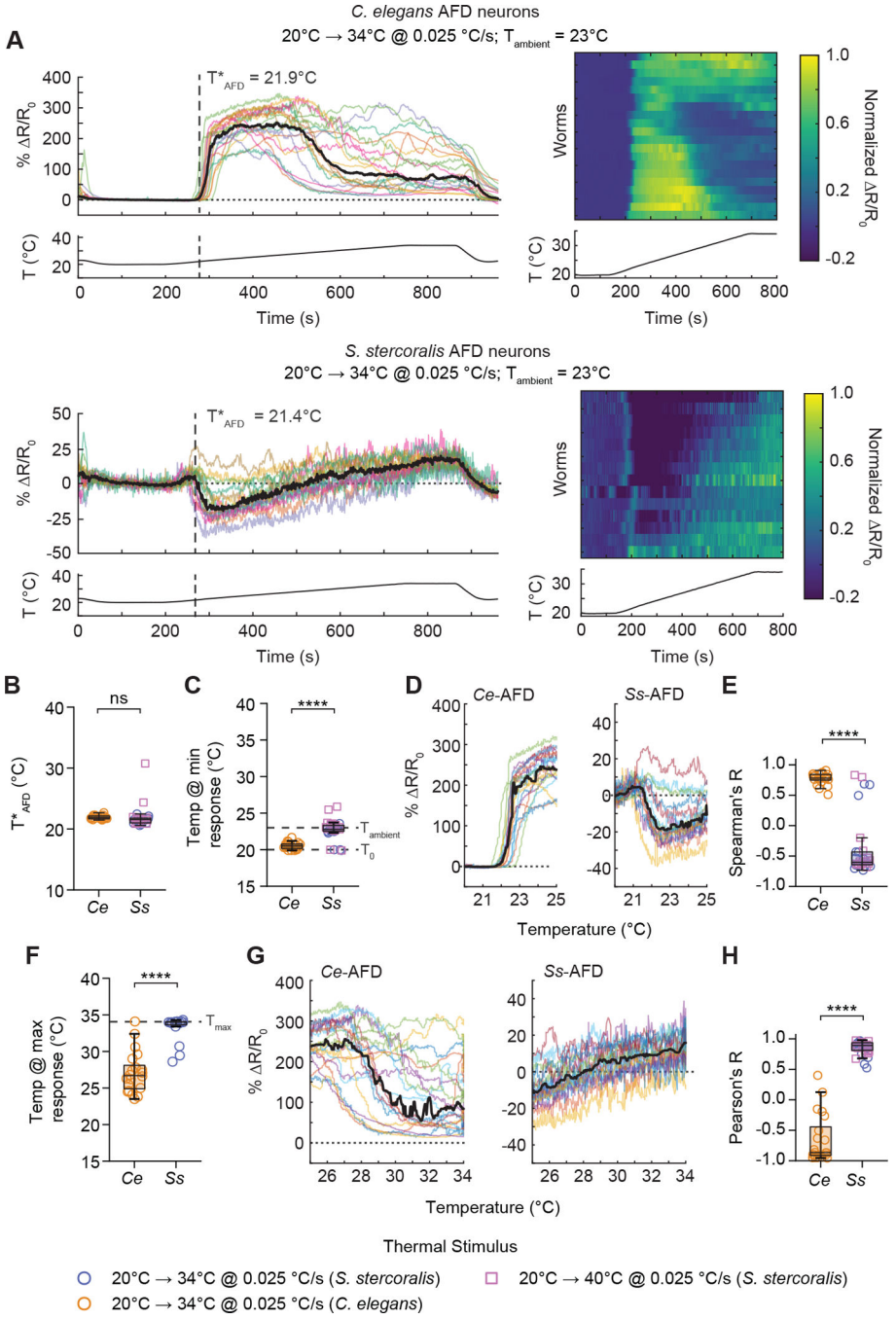

Figure 2. Warming ramps drive parasite-specific warming-triggered hyperpolarizations followed by near-linear thermal encoding in *S. stercoralis* AFD neurons.

A. *C. elegans* AFD and *S. stercoralis* AFD responses to a 20–34°C warming temperature ramp that approximates the temperatures experienced by iL3s migrating from ambient to human skin temperature (~34°C). Colored traces show the responses of individual worms; black traces show median responses. Horizontal dotted lines indicate response at baseline (R_0, 20°C). Heatmaps show responses normalized to the maximum $\Delta R/R_0$ response for each species, with R_0 set to zero. Responses are ordered by hierarchical cluster analysis. For

all plots, temperature traces show the average recorded temperature (mean in solid line, SD in shading; in some cases, shading is too small to be visible). Warming ramp slope = 0.025 °C/s. n = 15 worms for *S. stercoralis*, 20 for *C. elegans*. See also Figure S4, Figure S5. **B.** Thermal threshold (T^*_{AFD}) of *C. elegans* and *S. stercoralis* AFD calcium responses, where T^*_{AFD} is defined as the first temperature where $\Delta R/R_0$ is significantly different from baseline (3 * STD R_0) for at least 10 seconds. Data are responses to either a 20–34°C (circles) or a 20–40°C (squares) warming ramp. Meaningful differences between *C. elegans* T^*_{AFD} and *S. stercoralis* T^*_{AFD} were not detected (difference between median T^*_{AFD} = −0.325°C (*Ss*-AFD vs *Ce*-AFD), effect size = 0.072, power = 0.057, Mann-Whitney test). **C.** Temperature that elicits the lowest (*i.e.*, minimum or most negative) calcium response in *Ce*-AFD and *Ss*-AFD, in response to either a 20–34°C (circles) or a 20–40°C (squares) warming ramp. Horizontal dashed lines indicate $T_{ambient}$ (23°C) and T_0 (20°C). ****p<0.0001, Mann-Whitney test. **D.** Plots of % $\Delta R/R_0$ as a function of temperature at near-ambient temperatures (20–25°C). Horizontal dotted line indicates R_0 (response at 20°C). **E.** Quantification of monotonic correlation between temperature and calcium responses in the 20–25°C range. Values are Spearman's correlation coefficients. ****p<0.0001, Mann-Whitney test. **F.** Temperature that elicits the highest calcium response in *Ce*-AFD and *Ss*-AFD, in response to a 20–34°C warming ramp. Horizontal dashed line indicates the maximum temperature tested (T_{max}, 34°C). ****p<0.0001, Mann-Whitney test. n = 15 worms for *S. stercoralis*, 20 for *C. elegans*. **G.** Plots of % $\Delta R/R_0$ as a function of temperature at above-ambient temperatures (25–34°C). Horizontal dotted line indicates R_0 (response at 20°C). **H.** Quantification of linear correlation between temperature and calcium responses at 25°C and higher. Values are Pearson's correlation coefficients. ****p<0.0001, Mann-Whitney test. For all plots: icons indicate responses of individual worms, boxes show medians and interquartile ranges, whiskers show min and max values. $T_{ambient}$ (*i.e.*, the temperature that corresponds to both the cultivation temperature and the holding temperature) = 23°C. n = 20 worms for *C. elegans*, 30 for *S. stercoralis*, unless otherwise specified. All Mann-Whitney tests are two-sided.

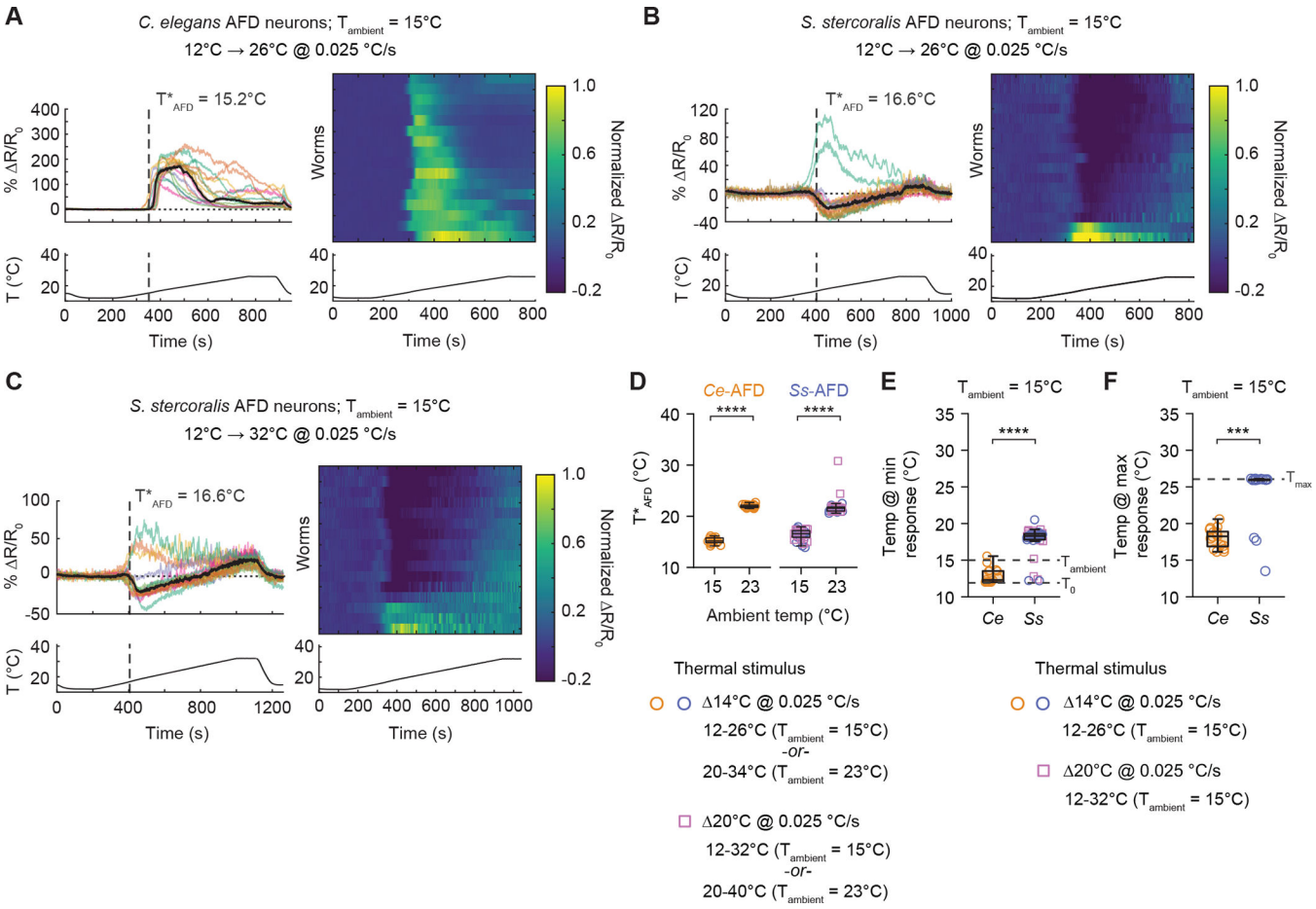

Figure 3. Exposure to a new ambient temperature shifts the *Ss*-AFD thermal threshold.

A. *Ce*-AFD responses to a 12–26°C temperature ramp, after overnight cultivation at 15°C and exposure to a holding temperature of 15°C. *Left:* Colored traces show the responses of individual worms; black traces show the median response. Horizontal dotted line indicates the baseline (R_0) response at 12°C. *Right:* Heatmap shows responses normalized to the maximum *Ce*-AFD $\Delta R/R_0$ response, with R_0 set to zero. Temperature traces show the average recorded temperature (mean in solid line, SD in shading; in some cases, shading is too small to be visible). Warming ramp slope = 0.025 °C/s. n = 16 worms. See also Figure S4. **B.** *Ss*-AFD responses to a 12–26°C temperature ramp, after overnight cultivation and holding at 15°C. Heatmap shows responses normalized to the second largest *Ss*-AFD $\Delta R/R_0$ response, with R_0 set to zero; the largest response is saturated. All other conventions are as in panel **A**. n = 17 worms. **C.** *Ss*-AFD responses to a 12–32°C temperature ramp, after overnight cultivation and holding at 15°C. Heatmap shows responses normalized to the maximum *Ss*-AFD $\Delta R/R_0$ response, with R_0 set to zero. All other conventions are as in panel **A**. n = 16 worms. **D.** Effect of ambient temperature (15°C versus 23°C) on *Ce*-AFD and *Ss*-AFD thermal threshold (T^*_{AFD}). Data are responses to ramps with a net temperature change of 14°C (circles) or 20°C (squares). n = 16 worms (*Ce*-AFD, $T_{ambient}$ = 15°C), 20 worms (*Ce*-AFD, $T_{ambient}$ = 23°C), 33 worms (*Ss*-AFD, $T_{ambient}$ = 15°C), 30 worms (*Ss*-AFD, $T_{ambient}$ = 23°C). ****p<0.0001, 2-way ANOVA with Tukey's multiple comparisons tests. Responses for $T_{ambient}$ = 23°C are re-plotted from Figure 2. **E.** Temperature that

elicits the lowest calcium response in *Ce*-AFD and *Ss*-AFD, in response to either a 12–26°C (circles) or a 12–32°C (squares) warming ramp. $T_{ambient}$= 15°C. Horizontal dashed lines indicate $T_{ambient}$ (15°C) and T_0 (12°C). n = 16 worms (*Ce*-AFD), 33 worms (*Ss*-AFD). ****p<0.0001, two-sided Mann-Whitney test. **F.** Temperature that elicits the highest calcium response in *Ce*-AFD and *Ss*-AFD, in response to a 12–26°C warming ramp. $T_{ambient}$ = 15°C. Horizontal dashed line indicates T_{max} (26°C). n = 16 worms (*Ce*-AFD), 17 worms (*Ss*-AFD). ***p<0.001, two-sided Mann-Whitney test. For all plots: icons indicate individual worms, boxes show medians and interquartile ranges, whiskers show min and max values.

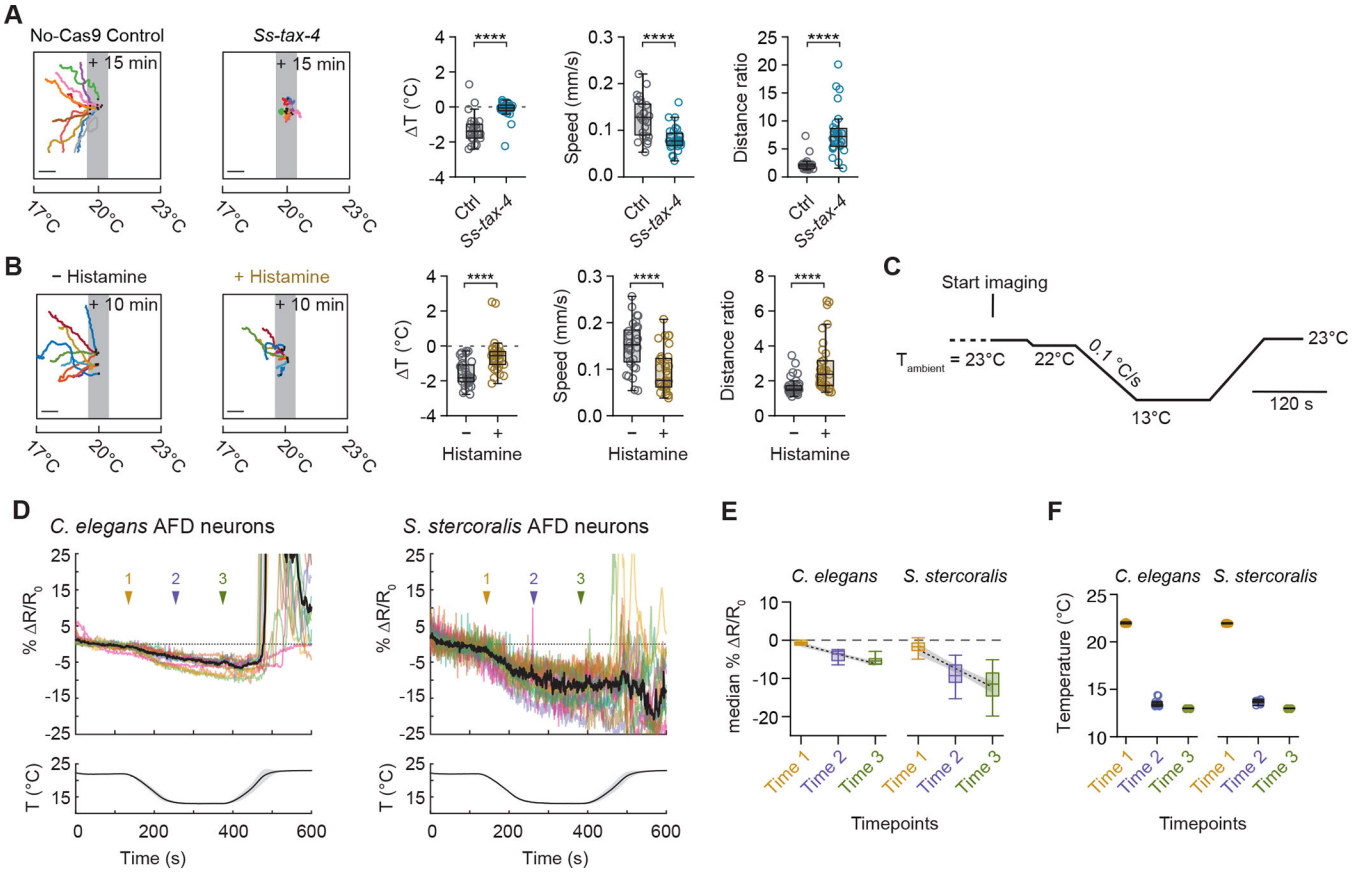

Figure 4. *S. stercoralis* iL3 negative thermotaxis is dependent on TAX-4 signaling and *Ss*-AFD activity.

A. CRISPR/Cas9 targeting of the *Ss-tax-4* gene results in iL3s with reduced negative thermotaxis behavior. *Left*: Tracks of no-Cas9 control iL3s and *Ss-tax-4* iL3s migrating for 15 min in a ~17–26°C gradient. T_{start} = 20°C. T_C = 23°C. Black dots indicate starting location of each worm. Scale bar = 2 cm, gray zone = 1°C centered at T_{start}. A subset of 10 randomly selected tracks is plotted and only a portion of the full gradient is shown. *Right*: Changes in temperature, average speed, and distance ratio exhibited by individual iL3s. Icons indicate individual worms, boxes show medians and interquartile ranges, whiskers show min and max values. n = 26 worms/single-worm assays (no-Cas9 control, "Ctrl"), 27 worms/single-worm assays (*Ss-tax-4*); ****p<0.0001, Mann-Whitney test. See also Figure S6. **B.** HisCl1-mediated silencing of *S. stercoralis* AFD induces deficits in negative thermotaxis. *Left:* Tracks of *Sr-gcy-23.2p*::*strHisCl1*; *Srgcy-23.2p*::*GFP* iL3s treated with BU saline or BU saline + 20–50 mM histamine for at least 2 h, migrating in a ~17–26°C gradient for 10 min. T_{start} = 20°C. T_C = 23°C. Figure conventions are as in panel **A**. *Right*: Change in temperature, average speed, and distance ratio exhibited by individual iL3s. n = 32 worms (BU treated; 3 assays, across 3 days), 33 worms (histamine treated; 4 assays, across 3 days); ****p<0.0001, Mann-Whitney test. **C.** Diagram of a cooling stimulus spanning the range of temperatures eliciting strong negative thermotaxis in *S. stercoralis* iL3s (22–13°C). Ramp slope: −0.1 °C/s. See also Figure S3. **D.** *Ce*-AFD and *Ss*-AFD responses to the rapid 22–13°C cooling temperature ramp shown in panel **C.** Colored traces

show the responses of individual worms; black traces show median responses. Horizontal dotted lines indicate baseline (R_0) responses at 22°C. Arrowheads indicate timepoints shown in panels **E-F**. **E.** Simple linear regression of *Ce*-AFD and *Ss*-AFD response magnitude at regularly spaced timepoints during a 22–13°C temperature ramp. Time 1 is +220 s of continuous fluorescent illumination; subsequent timepoints are each an additional +120 s. Boxes show medians and interquartile ranges, whiskers show min and max values. Dashed lines show best-fit linear regression line, gray shading shows 95% confidence intervals. *Ce*-AFD regression equation: $Y = -0.021*X + 3.59$, $R^2 = 0.70$; replicates test for lack of fit: discrepancy (F) = 1.96, $p = 0.17$. *Ss*-AFD regression equation: $Y = -0.041*X + 6.60$, $R^2 = 0.61$; replicates test for lack of fit: discrepancy (F) = 4.56, $p < 0.05$. **F.** The change in temperature across the timepoints used for measurements in panel **E** is non-linear. Icons indicate the responses of individual worms, boxes show medians and interquartile ranges, whiskers show min and max values. For **D-F**, n = 14 worms (*Ce*-AFD), 15 worms (*Ss*-AFD).

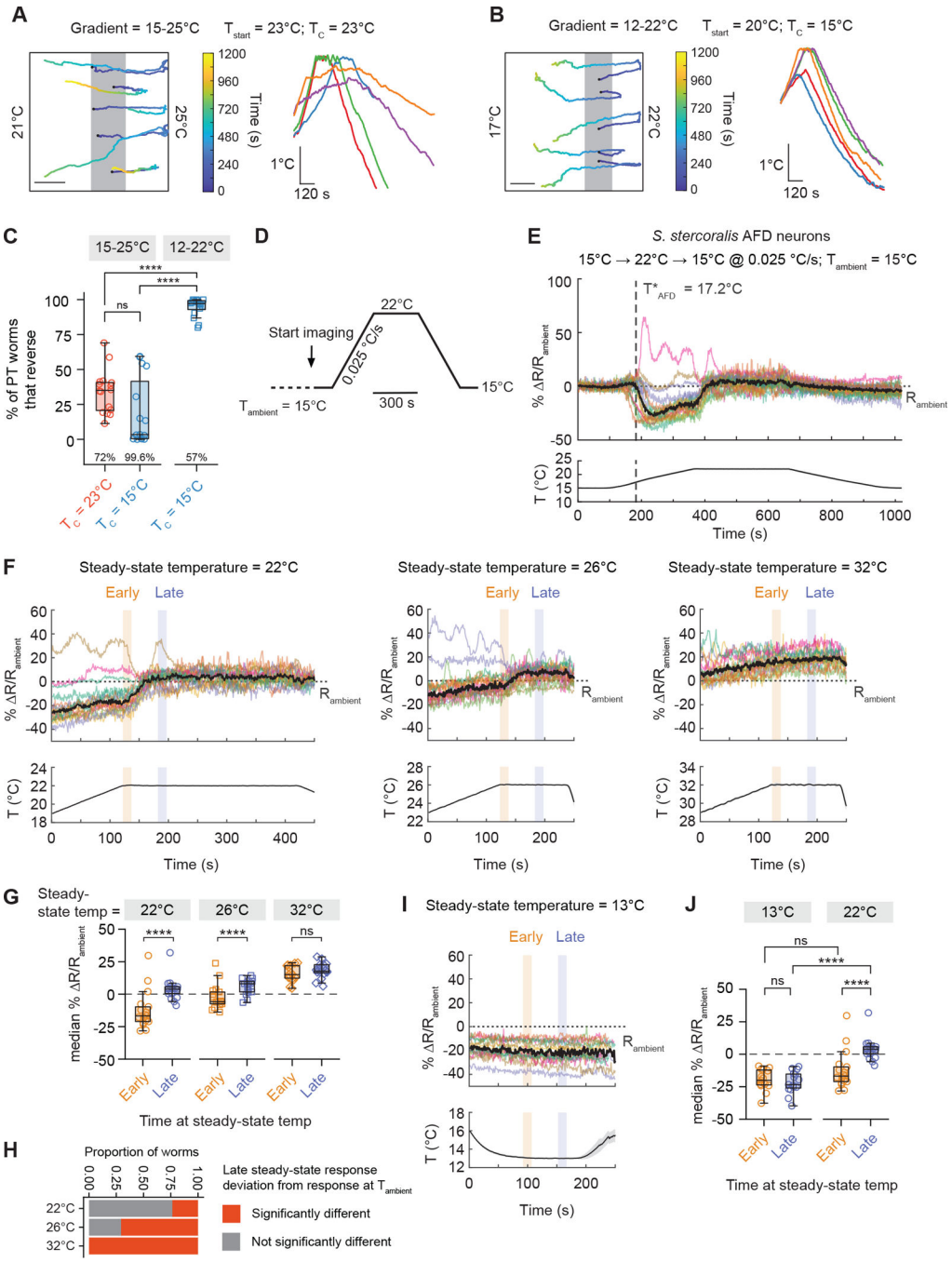

Figure 5. *S. stercoralis* iL3s display rapid behavioral and neural adaptation in response to thermosensory cues well below host body temperatures.

A. Example tracks of individual *S. stercoralis* iL3s displaying a "U-turn" thermotaxis behavior comprised of an abrupt transition from sustained positive thermotaxis to sustained negative thermotaxis. Gradient range: 15–25°C. T_{start} = 23°C. T_C = 23°C. Left: Example worm tracks artificially distributed along the y-axis to increase visual clarity. Black dots indicate the starting positions of the worms. Only a portion of the full gradient is shown. Track color indicates time during the assay. Right: Temperatures experienced by individual

iL3s as a function of time; traces are the same worms displayed in the left panel. Median time spent near the maximum temperature reached by each worm = 216 s (IQR = 166–244 s). n = 5 worms. **B.** When cultivation temperature is 15°C, worms also display U-turn behaviors. Gradient range: 12–22°C. T_{start} = 20°C. T_C= 15°C. Median time spent near the maximum temperature reached by each worm = 126 s (IQR = 106–150 s). n = 9 worms, plots show subset of tracks. Plots use same conventions as in panel **A**. **C.** Percent of *S. stercoralis* iL3s engaging in positive thermotaxis (PT) that U-turn into negative thermotaxis. Annotations along the x-axis are the average percentage of the total population that engages in positive thermotaxis under each experimental condition. Boxes indicate medians and interquartile ranges; whiskers indicate min and max values. T_{start} = 23°C for the 15–25°C gradient and 20°C for the 12–22°C gradient. n = 15 assays for the 15–25°C gradient when T_C = 15°C, 16 for all other conditions. ns = not significant (p=0.47), ****p<0.0001, Kruskal-Wallis test with Dunn's post-test. **D.** Diagram of a thermal stimulus that mimics temperature ramps experienced by 15°C-cultivated iL3s that perform thermotaxis U-turns in a 12–22°C gradient. These parameters were chosen because they are the assay conditions most likely to elicit a U-turn behavior. Ramp slope: ±0.025 °C/s. Holding time at 22°C = 5 min. **E.** *Ss*-AFD calcium responses to the thermal stimulus shown in panel **D.** For calcium responses, colored lines indicate responses from individual worms, black line indicates median response. Temperature traces are mean ± SD recorded temperature (lines + shading; in some cases, shading is too small to be visible). Dashed vertical line indicates thermal threshold. Dotted horizontal line indicates the response at ambient ($R_{ambient}$); $T_{ambient}$ = 15°C. n = 17 worms. **F.** *Ss*-AFD calcium responses to different steady-state temperatures: 22°C, 26°C, and 32°C. Colored shading indicates time windows used for analyses in panels **G**, **H**, and **J**. n = 17 worms (22°C or 26°C), 16 worms (32°C). All other conventions are the same as panel **E**. **G.** Adaptation of *Ss*-AFD calcium responses at different steady-state temperatures. Calcium responses are calculated over two analysis windows: Early (first 15 seconds) and Late (15 seconds following 1 min at the steady-state temperature). ns = not significant (p=0.32), ****p<0.0001, two-way repeated-measures ANOVA with Šidák's multiple comparisons tests; multiplicity adjusted p values are reported. Boxes indicate medians and interquartile ranges; whiskers indicate min and max values. n = 17 worms (22°C or 26°C), 16 worms (32°C). $T_{ambient}$ = 15°C. **H.** Temperature stimuli that are more likely to result in thermotaxis U-turns (*i.e.,* when the maximum temperature reached by the thermal ramp is 22°C or 26°C vs 32°C) result in a higher proportion of steady-state adaptation responses such that Late window responses are not significantly different from responses at $T_{ambient}$. For each worm, significant steady-state responses are those that vary from the average $T_{ambient}$ response by at least 3 standard deviations. 22°C vs 26°C: p=0.045; 26°C vs 32°C: p=0.13; 22°C vs 32°C: p<0.0001, Fisher's exact tests with Bonferroni-Dunn correction for multiple comparisons. $T_{ambient}$ = 15°C. All statistical tests are two-sided; when possible, we report multiplicity adjusted p values. **I**. *Ss*-AFD calcium responses to steady-state stimulation at 13°C following a 22–13°C cooling temperature ramp (Figure 4C). Trace is a subset of the full response shown in Figure 4D, re-normalized to the response at 23°C. Colored shading indicates time windows used for analysis. n = 15 worms. $T_{ambient}$ = 23°C. **J**. *Ss*-AFD steady-state responses at 22°C (following a 15–22°C warming temperature ramp) and 13°C (following a 22–13°C cooling temperature ramp), at Early (first 15 s) and Late (15 s after 1 min at steady-state temp) time windows.

Responses at 22°C following a 15–22°C warming temperature ramp are replotted from panel **G**. For responses at 22°C, $T_{ambient}$ = 15°C; for responses at 13°C, $T_{ambient}$ = 23°C. Despite displaying similar initial magnitudes (early 13°C vs. early 22°C), only the warming-triggered hyperpolarization response at 22°C displays rapid adaptation (early 22°C vs late 22°C); cooling-triggered hyperpolarizations at 13°C are constant across the stated time windows (early 13°C vs late 13°C). ns = not significant (early 13°C vs. early 22°C, p=1; early 13°C vs late 13°C, p=0.46), ****p<0.0001, two-way repeated-measures ANOVA with Šidák's multiple comparisons tests and Bonferroni-Dunn correction; multiplicity adjusted p values are reported. Values are median % $\Delta R/R_{ambient}$. Boxes are median and interquartile range; whiskers indicate min and max values. n = 15 worms (13°C), 17 worms (22°C).

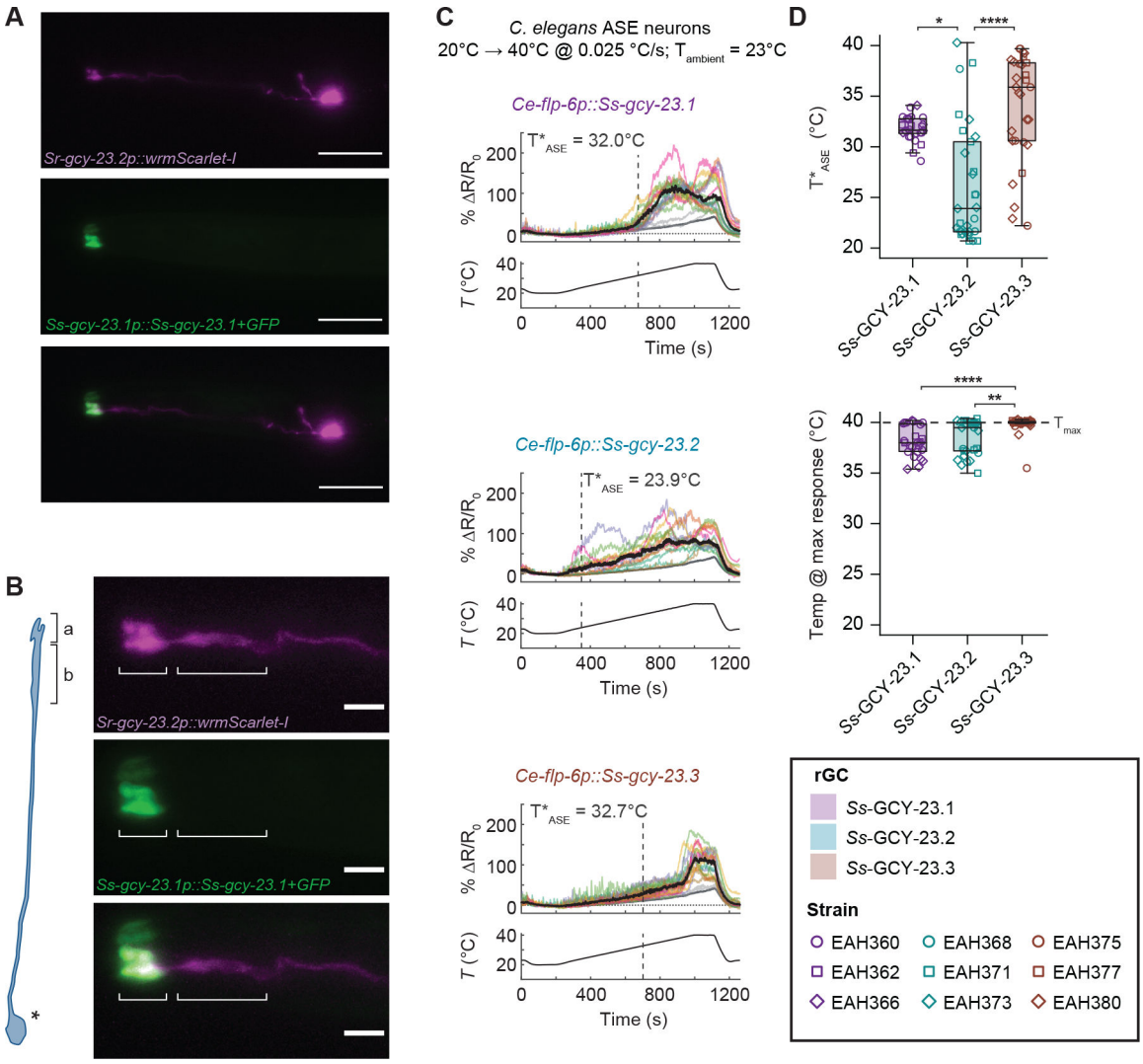

Figure 6. All three *S. stercoralis* AFD-specific rGCs are thermoreceptors.

A. A GFP-tagged version of *Ss*-GCY-23.1 under the control of the *Ss-gcy-23.1* promoter region localizes to the *Ss*-AFD sensory tip. Images show *Ss-gcy-23.1p::Ss-gcy-23.1-GFP* (green) co-expressed with a cell-filling marker (*Sr-gcy-23.2p::wrmScarlet-I*, magenta) in a *S. stercoralis* iL3. Asterisk indicates a single *Ss*-AFD cell body; closed arrowhead indicates the sensory tip of the filled neuron. Open arrowhead indicates the location of the second *Ss*-AFD neuron, which only expresses *Ss*-GCY-23.1-GFP. Scale bar is 20 μm; anterior is to the left. **B.** The portion of the *Ss*-AFD process with a lamellar structure appears to contain multiple zones: an anterior region with extensive lamellae (a), and a more posterior region with less complex lamellar structures (b); *Ss*-GCY-23.1 localizes specifically to the more anterior region. Left: outline of the full *Ss*-AFD neuron shown in panel **A**. Asterisk indicates cell body. Right: Magnified view of images shown in panel **A**. Labels indicate *Ss*-AFD lamellar process with (a) and without (b) expression of *Ss*-GCY-23.1. Scale bar is 5 μm; anterior is to the left. **C.** Responses of *C. elegans* ASER/L neurons expressing YC3.60 and *Ss*-GCY-23.1 (top), *Ss*-GCY-23.2 (middle), or *Ss*-GCY-23.3 (bottom) to warming temperature ramps. Warming stimulus ramp: 20–40°C at

0.025 °C/s. Vertical dashed lines indicate average thermal threshold (T^*_{ASE}), defined as the first temperature where $\Delta R/R_0$ deviates from the average *Ce*-ASE_{WT} response by at least 3 * STD for a minimum of 40 s. Colored traces indicate responses of individual worms that crossed the thermal threshold; light gray traces indicate responses that did not. Thick black traces show median responses; only worms with a response above threshold are included in averages. Thick dark gray traces show median response of wild-type *Ce*-ASER/L neurons (Figure S7B). Temperature traces show the average ± SD recorded temperature (lines + shading; in some cases, shading is too small to be visible). R_0 (horizontal dotted lines) = response at 20°C. $T_{ambient}$ = 23°C. n = 15 worms above threshold out of 17 total worms (*Ss*-GCY-23.1, Strain EAH360), 15 of 15 worms (*Ss*-GCY-23.2, Strain EAH373), and 17 of 19 worms (*Ss*-GCY-23.3, Strain EAH380). See also Figure S7. **D.** Thermal thresholds (upper) and temperatures eliciting highest calcium responses (lower) for *C. elegans* ASE neurons expressing *Ss*-GCY-23.1 (purple icons), *Ss*-GCY-23.2 (teal icons), and *Ss*-GCY-23.3 (red icons) measured in individual worms from three replicate strains (n = 5–17 worms per strain). Only worms with a response crossing the thermal threshold are included in quantifications. Boxes show medians and interquartile ranges, whiskers show min and max values. Horizontal dashed line indicates T_{max} (40°C). n = 5–17 worms per strain, with 26, 30, and 34 worms per genotype (*Ss*-GCY-23.1, *Ss*-GCY-23.2, and *Ss*-GCY-23.3, respectively). *p<0.05, **p<0.005, ****p<0.0001, two-sided Kruskal-Wallis test with Dunn's post-test; multiplicity adjusted p values are reported.

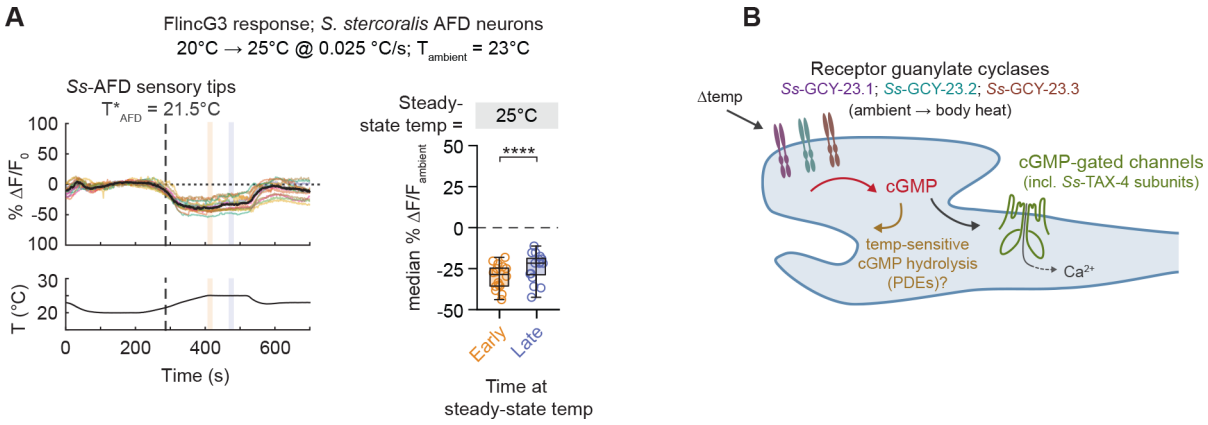

Figure 7. Warming-triggered inhibition in *Ss*-AFD reflects a reduction in cGMP levels.

A. Fluorescent response (% $\Delta F/F_0$) of the cGMP biosensor FlincG3 in the *Ss*-AFD sensory tips during a 20–25°C temperature ramp. *Left:* Colored traces show the responses of individual worms; black traces show median responses. Ramp speed: 0.025 °C/s. F_0 (horizontal dotted lines) = response at 20°C. n = 16 worms. *Right:* cGMP levels display rapid adaptation at near-ambient warm temperatures. Plot shows median FlincG3 responses in Ss-AFD during steady-state application of an above-ambient stimulus (25°C), at early (first 15 s) and late (15 s after 1 min at 25°C) temporal windows. Values are normalized to the response at $T_{ambient}$. Boxes are medians and interquartile ranges; whiskers indicate min and max values. ****p<0.0001, Wilcoxon matched-pairs signed rank test. **B.** Proposed schematic of thermotransduction in *Ss*-AFD. Three *Ss*-AFD-specific receptor-type guanylate cyclases (*Ss*-GCY-23.1, *Ss*-GCY-23.2, *Ss*-GCY-23.3) act as thermoreceptors to sense changes in temperature from ambient to mammalian body heat. *Ss*-AFD-rGCs increase levels of cGMP after exposure to above-ambient temperatures. Exposure to warming stimuli near ambient temperatures results in the reduction of cGMP levels through the activity of unknown proteins, potentially temperature-dependent phosphodiesterases (PDEs). *Ss*-AFD cGMP levels are transduced into Ca^{2+} flux by a cGMP-gated cation channel that includes the subunit *Ss*-TAX-4, which is required for thermotaxis behaviors of iL3s.

KEY RESOURCES TABLE

REAGENT or RESOURCE	SOURCE	IDENTIFIER
Bacterial and virus strains		
Escherichia coli: Strain OP50	*Caenorhabditis* Genetics Center	OP50
Experimental models: Organisms/strains		
Caenorhabditis elegans: Strain N2	*Caenorhabditis* Genetics Center	N2
Caenorhabditis elegans: Strain IK890	Dr. Ikue Mori	
Caenorhabditis elegans: Strain XL115	Dr. Shawn Lockery	
Meriones unguiculatus: Mongolian	Charles River Laboratories	Gerbils
See Table S3 for *Caenorhabditis elegans* strain generated for this study.	N/A	N/A
Chemicals, peptides, and recombinant proteins		
Histamine dihydrochloride	Sigma-Aldrich	H7250–10G
Halocarbon oil 700	Sigma-Aldrich	H8898–50ML
Oligonucleotides		
GTAACATTTGACTTGATGGGTGG	[46]	*Ss-tax-4* CRISPR target sequence
See Table S4 for primer sequences.	N/A	N/A
Recombinant DNA		
See Table S2 for plasmid descriptions.	N/A	N/A
Software and algorithms		
GraphPad Prism 9	GraphPad	http://www.graphpad.com
Zeiss ZEN pro v2.6	Carl Zeiss	https://www.zeiss.com/microscopy/us/products/microscope-software/zen.html
FIJI	[80]	https://fiji.sc/
Geneious Prime 2022.0.1	Biomatters	https://www.geneious.com
MATLAB R2019B	MathWorks	https://www.mathworks.com/products/matlab.html
ATEC302 TEC controller	Accuthermo Technology	http://www.accuthermo.com/
G*Power 3.1	[82]	https://www.psychologie.hhu.de/arbeitsgruppen/allgemeine-psychologie-und-arbeitspsychologie/gpower
R 4.1.2	The R Foundation	https://www.r-project.org/
Ggplot v3.3.5	[83]	ggplot
Other		
Annular-style Peltier element	Laird Thermal Systems	430533–502
Temperature-controlled recirculating water bath	Fisher Scientific	13–874-180
PID controller	Accuthermo Technology	ATEC302
H-bride amplifier	Accuthermo Technology	FTX700D
AC/DC power converters	TDK-Lambda Americas Inc	LS35–12
10 kΩ thermistor	Littelfuse	USP12837

REAGENT or RESOURCE	SOURCE	IDENTIFIER
M9 solution (3 g KH2PO4, 6 g Na2HPO4, 5 g NaCl, 1 mL 1 M MgSO4, dH2O to 1 L)	[65]	M9 solution
BU saline (7.10 g Na2HPO4, 2.99 g KH2PO4, 4.09 g NaCl, dH2O to 1 L)	[79]	BU saline
See Table S5 for all thermal stimulus protocols.	N/A	N/A
Archived GitHub repository containing all data, original code, and hardware details.	Zenodo	DOI: 10.5281/zenodo.6385743